



1 An internal solitary wave forecasting model in the northern South 2 China Sea (ISWFM-NSCS)

3 Yankun Gong¹, Xueen Chen², Jiexin Xu¹, Jieshuo Xie¹, Zhiwu Chen¹, Yinghui He¹, Shuqun Cai^{1,3,4}

4 ¹State Key Laboratory of Tropical Oceanography, South China Sea Institute of Oceanology, Chinese Academy of Sciences,
5 Guangzhou 510301, China

6 ²College of Oceanic and Atmospheric Sciences, Ocean University of China, Qingdao, 266100, China

7 ³Institution of South China Sea Ecology and Environmental Engineering, Chinese Academy of Sciences, Guangzhou 510301,
8 China

9 ⁴University of Chinese Academy of Sciences, Beijing, 100049, China

10 *Correspondence to:* Shuqun Cai (caisq@scsio.ac.cn)

11 **Abstract.** Internal solitary waves (ISWs) are a ubiquitous phenomenon in the dynamic ocean system, which play a crucial role
12 in driving transport through turbulent mixing. Over the past few decades, numerical modelling became a vital approach to
13 investigate the generation mechanism and spatial distribution of ISWs. The northern South China Sea (NSCS) has been treated
14 as a physical oceanographic focus of ISWs in massive numerical studies since last century. However, there was no systematic
15 evaluation of a reliable three-dimensional model about accurately reproducing ISW characteristics in the NSCS. In this study,
16 we implement a three-dimensional ISW forecasting model in the NSCS and quantitatively evaluate the requirements of factors
17 (i.e., model resolution, tidal forcing, and stratification selection) in precisely depicting ISW properties by comparing with
18 observational data at a mooring station in the vicinity of the Dongsha Atoll. Firstly, the 500 m-resolution model can basically
19 reproduce the principal ISW characteristics, while the 250 m-resolution model would be a better solution to identify wave
20 properties, specifically increasing 40% accuracy of predicting characteristic half-widths. Nonetheless, a 250 m-resolution
21 model spends nearly fivefold computational resources of a 500 m-resolution model in the same model domain. Compared with
22 the former two, the model with a lower resolution of 1000 m severely underestimates the nonlinearity of ISWs, resulting in an
23 incorrect ISW field in the NSCS. Secondly, the model with eight (or thirteen) primary tidal constituents can accurately
24 reproduce the real ISW field in the NSCS, while the one with four main harmonics (M2, S2, K1 and O1) would underestimate
25 averaged wave-induced velocity for about 38% and averaged mode-1 wave amplitude for about 15%. Thirdly, the model with
26 the initial condition of field-extracted stratification gives a better performance in predicting some wave properties than the
27 model with climatological stratification, namely 13% improvement of arrival time and 46% improvement of characteristic
28 half-width. Finally, background currents, spatially varying stratification and external (wind) forcing are discussed to reproduce
29 a more realistic ISW field in the future numerical simulations.



30 1 Introduction

31 Numerical simulations, one of the most important approaches to investigate internal solitary waves (ISWs) in the world's
32 oceans, have been gradually developed from two-dimensional (e.g., Du et al., 2008; Buijsman et al., 2010) to three-dimensional
33 (e.g., Zhang et al., 2011; Alford et al., 2015) over the past few decades. South China Sea (SCS), the largest marginal sea in the
34 northwest Pacific, has been commonly known as an active region of ISWs via massive in-situ observations (cf. Ramp et al.,
35 2004, 2019; Farmer et al., 2009, 2011) and numbers of remote sensing images (cf. Liu et al., 2004; Zheng et al., 2001, 2007).
36 Although the vertical structure and horizontal distribution on the sea surface of ISWs can be nicely illustrated by field
37 measurements at sparse sites and satellite images, respectively, they are still of limited value for telling a complete story of
38 ISWs in the entire northern SCS (NSCS). Complementary to in-situ and remote-sensing observations, numerical model can
39 give a comprehensive characterization in the ISW field in case of realistic initial and boundary conditions. Hence, we take
40 NSCS as an example to introduce a high-performance ISW forecasting model and quantitatively evaluate requirements of
41 model configurations (i.e., resolution, tidal forcing, and stratification selection) for accurately reproducing a real ISW field.

42 With the development of higher performance computing facilities, a variety of three-dimensional (3D) realistic numerical
43 models with structured and unstructured grids were established for simulating ISWs in the NSCS (see Table 1), such as
44 MITgcm (Vlasenko et al., 2010), SUNTANS (Zhang et al., 2011) and FVCOM (Lai et al., 2019). Meanwhile, the model
45 capabilities have been continuously improved (Simmons et al., 2011). Specifically, the model resolution was effectively
46 enhanced from 250-1000 (Δx - Δy) m (Guo et al., 2011) in a limited domain to 150/300 m in a large domain including the entire
47 NSCS (Zeng et al., 2019). From past to present, the barotropic tidal forcing dataset TOPEX/Poseidon Solution (TPXO, Egbert
48 and Erofeeva, 2002) and climatological stratification dataset World Ocean Atlas (WOA, Locarnini et al., 2018) have been
49 updated with higher resolutions both in horizontal and vertical, providing more realistic and precise boundary and initial
50 conditions in the model configurations. Although it is commonly known that a higher-resolution model can tell a more
51 complete story of ISWs, the usage of computational resources is worthy to be considered. Thus, what resolution of model is
52 needed to give an accurate depiction of ISW fields and simultaneously save the computational cost is still a question.

53 Even though numbers of previous in-situ observations have shown the four barotropic tidal constituents (M2, K1, O1 and
54 S2) are dominant at the Luzon Strait (Zhao and Alford, 2006; Farmer et al., 2009), the other barotropic tidal constituents (e.g.,
55 N2, K2, P1 and Q1) are also non-negligible (Beardsley et al., 2004). Historically, numerical simulations with different numbers
56 of tidal constituents have been widely employed to investigate the physical dynamics of ISWs in the NSCS, i.e., single K1
57 harmonic (Li, 2014), four tidal harmonics (Buijsman et al., 2010), and eight primary tidal harmonics (Alford et al., 2015; Jin
58 et al., 2021). Among these, eight tidal constituents were most commonly applied in the 3D models. However, other tidal
59 constituents, such as M4, MS4, MN4, MM, and MF, were yet to be considered. The questions that arise are whether a single
60 tidal constituent can satisfy the reproduction of a real ISW field and how many tidal constituents are required for running an
61 accurate 3D realistic ISW model.



62 Apart from resolution and tidal forcing, stratification selection is also an important factor in improving model accuracy. A
63 horizontally homogenous stratification profile was normally implemented as an initial condition in a 3D realistic model (cf.
64 Zhang et al., 2011; Lai et al., 2019). Specifically, a domain average of the climatological dataset (WOA) is one of the most
65 common options (Vlasenko et al., 2010; Zeng et al., 2019), since the in-situ observational data are relatively inaccessible. Once
66 the field data at an isolated mooring station are available, are they a better choice than the climatological data to be the model's
67 initial condition? What if the mooring is near-field (in the vicinity of the Luzon Strait, the ISW generation site) or far-field
68 (e.g., in the deep basin or over the continental slope and shelf)?

69 In this paper, we attempt to introduce a high-performance ISW forecasting model and evaluate the roles of different
70 resolutions, initial and boundary conditions in accurately reproducing ISWs via a series of sensitivity 3D non-hydrostatic
71 numerical simulations. The paper is structured as follows. In section 2, configurations of the 3D forecasting model are
72 introduced, as well as the simultaneous remote sensing images and in-situ observations. The model calibrations are presented
73 in section 3. In section 4, we quantitatively illuminate the requirements of model resolutions, tidal constituents, and initial
74 stratification selection for a reliable 3D ISW forecasting model. Discussion and conclusions follow in section 5.

75 **2 Data and Methods**

76 To characterize the real ISW field in the NSCS, we implement an ISW forecasting model (ISWFM-NSCS) and compare the
77 modelled wave properties on the continental slope with those observed at in-situ mooring station DS (marked as magenta star
78 in Fig. 1a). Remote sensing images are downloaded for the model calibration as well.

79 **2.1 Numerical modelling**

80 Although running a 2D slice model is much more economical than running a 3D model from the perspective of
81 computational resources, the 2D model cannot correctly reproduce the ISW field in the real ocean (see Appendix A). Therefore,
82 we implement a realistic 3D non-hydrostatic primitive equation ocean solver (MIT general circulation model, MITgcm,
83 Marshall et al., 1997) in the spherical coordinate to reproduce the ISWs features in the NSCS. The model domain (115.8° –
84 123.8° E, 17.8° – 22.3° N, see blue box in Fig. 1a) includes the main generation site of ISWs (i.e., Luzon Strait) and the mooring
85 station DS on the continental slope. Bathymetry data are derived from the global gridded bathymetry dataset GEBCO
86 (https://www.gebco.net/data_and_products/gridded_bathymetry_data). To keep the consistency with the instrumental
87 deploying period, we start the model from 00:00 UTC 5 August 2014 and last fifteen days. Previous statistical analyses, based
88 on SAR images in the NSCS from 1995 to 2001, also indicated that ISW occurrence frequencies were relatively high in August
89 (Zheng et al., 2007). The initial model temperature and salinity profiles (see black and blue lines in Fig. 1b) are derived from
90 the WOA18 climatology dataset (World Ocean Atlas 2018) by spatially averaging the monthly output in August, resulting in
91 horizontally-uniform conditions. Density and buoyancy frequency profiles are shown as black lines in Figs. 1c and 1d.



92 To ensure ISWs can be physically derived and consider the computational efficiency, the horizontal cell (Δx) is set as 500
93 m in both zonal and meridional directions. In order to satisfy the high-mode vertical resolution requirements, 90 vertical layers
94 are spaced in accordance with the hyperbolic tangent function (Stewart et al., 2017), namely ranging from 5 m near the surface
95 to 120 m near the sea bed (in the deep water). We impose a time step of $\Delta t = 10$ sec to satisfy the Courant-Friedrichs-Lewy
96 (CFL) conditions in both horizontal and vertical. The Coriolis parameter is constant in the entire model domain, which is given
97 by a value at a latitude of 20.5° ($f = 5.1 \times 10^{-5} \text{ rad s}^{-1}$). To determine whether non-hydrostatic mode is necessary, we also run
98 a hydrostatic model (not shown). It is noting that fake internal solitary-like wave trains, also called spurious non-hydrostatic
99 processes (Alvarez et al., 2019), are clearly visible at first glance, suggesting that hydrostatic mode is inappropriate for a high-
100 resolution model of ISWs. We therefore configure the model in non-hydrostatic mode.

101 The control run (Exp. 1, **500m_8HARs**) is driven by eight main tidal constituents (M2, S2, N2, K2, K1, O1, P1, and Q1) on
102 the four open boundaries with values originated from the Oregon State University TOPEX/Poseidon Solution (TPX08-atlas
103 data) with $1/30^\circ$ resolution (Egbert and Erofeeva, 2002). A 25 km wide sponge layer is imposed on each lateral boundary to
104 absorb internal wave energy and avoid wave reflection back to the inner region. Quasi-steady conditions occur after 3 days, so
105 the model results are analyzed over the remaining 12 days (8 – 20 August). The control run (**500m_8HARs**) runs at 1 h time
106 interval in the entire model domain and single-point outputs with a higher sampling rate of 1 min at the selected station DS for
107 recording the local ISW properties, and thereby comparing to the in-situ observations. Constant horizontal and vertical eddy
108 viscosity and diffusivity coefficients are imposed as $A_h = 0.5 \text{ m}^2 \text{ s}^{-1}$; $A_v = 5 \times 10^{-3} \text{ m}^2 \text{ s}^{-1}$; $K_h = 0.5 \text{ m}^2 \text{ s}^{-1}$; $K_v = 5 \times 10^{-3}$
109 $\text{m}^2 \text{ s}^{-1}$ to eliminate grid-scale instability (Legg and Huijts, 2006). The bottom stresses are parameterized using a quadratic law
110 with a bottom drag coefficient of $C_d = 2.5 \times 10^{-3}$.

111 2.2 Remote sensing images

112 Remote sensing imagery contains lots of detailed information of ISW properties, including wave crest lines and their arrival
113 time, which was commonly applied in the NSCS (Liu et al., 2004; Zheng et al., 2007). Here we download two MODIS true-
114 color pictures with a horizontal resolution of 250 m at 05:15 UTC on 14 August and at 02:50 UTC on 15 August 2014,
115 respectively. In addition, we compute the horizontal gradients of sea surface height ($|\nabla\eta|$, in the unit of cm km^{-1}), which detects
116 the variations in surface roughness caused by the ISW-induced convergent and divergent currents, thereby producing
117 analogous images to the satellite images. Note that the model is hourly sampled, so we select the closest snapshots of $|\nabla\eta|$ at
118 05:00 UTC on 14 August and at 03:00 UTC on 15 August 2014 to compare with MODIS images.

119 2.3 In-situ measurements

120 The through-water-column mooring station DS (magenta star in Fig. 1a) is located at $117^\circ 44.7' \text{E}$, $20^\circ 44.2' \text{N}$ in the vicinity
121 of the Dongsha Atoll, which was deployed at a water depth of ~ 1250 m from 1 August to 28 September 2014. Three acoustic
122 Doppler current profilers (ADCPs) measured currents ranging from a depth of 1180 m to the sea surface every two minutes



123 with 16-m vertical bins in upper 900 m and 8-m vertical bins below 900 m. The mooring was configured by temperature
124 sensors, conductivity-temperature-depth (CTD) sensors and conductivity-temperature (CT) sensors at different water depths.
125 The temperature sensors were at 10 m, 30 m, 50 m, 90 m, 130 m, 150 m, 170 m, 250 m, 350 m, 500 m, 600 m, 700 m, 800 m,
126 950 m, 1050 m, and 1220 m; the CTD sensors were at 1 m and 1100 m; and the CT sensors were at 20 m, 40 m, 70 m, 110 m,
127 150 m, 200 m, 300 m, 450 m, 550 m, 650 m, 750 m, 850 m, 1000 m, and 1200 m. Temporal sampling rates were 10 sec for
128 the temperature and CTD sensors, and 15 sec for the CT sensors, respectively. The instruments carried by the moorings
129 generally functioned well, but CT sensors stopped working after 6 September 2014 due to the lack of power. Besides, Xu et
130 al. (2020) indicated that an anti-cyclonic eddy dominated the region of the mooring since mid-September 2014, which
131 significantly affected the local wave properties at the DS station. To avoid the impacts of background currents, we selected
132 fifteen ISWs during the spring tidal period from 00:00 UTC 8 August to 00:00 UTC 15 August as criteria to quantitatively
133 evaluate the performance of sensitivity numerical experiments.

134 3 Model results and calibrations

135 In this section, we validate the model accuracy from three aspects: barotropic tidal constituents via comparing with TPXO8-
136 atlas dataset and in-situ observational data; spatial distributions of ISWs via comparing with the remote-sensing images; wave
137 properties (i.e., amplitude, arrival time, wave-induced velocity and propagation direction) of ISWs via comparing with the in-
138 situ observations at mooring station DS.

139 3.1 Barotropic tide calibrations

140 The 3D control run only runs for 15 days, which is too short to do the harmonic analysis. To validate the model accuracy in
141 simulating the barotropic currents of eight key tidal constituents, we rerun a 3D model (Exp. 2, *500m_8HARs_BT*) with the
142 same configurations as *500m_8HARs*, but extend the duration time to 100 days and turn off the iteration of temperature and
143 salinity to focus on the barotropic tide regimes.

144 As M2, S2, K1, and O1 barotropic tides are dominant in the NSCS (Ramp et al., 2004; Farmer et al., 2009), here we calculate
145 the amplitude (U) and phase (ϕ) of the zonal velocity (u_{bt}) by doing the harmonic analysis over the last 90 days in Exp. 2
146 (*500m_8HARs_BT*) and compare them with the TPXO8-atlas dataset. A root-mean-square error ($RMSE$), referring to
147 Cummins and Oey (1997), is computed to evaluate the model performance in the barotropic regime, which is given by

$$148 \quad RMSE_h = \sqrt{\frac{1}{2}[(U_m^2 + U_o^2) - U_m U_o \cos(\phi_m - \phi_o)]}, \quad (1)$$

149 in which, subscript h represent four different harmonics; U and ϕ are amplitude and phase of zonal barotropic currents with
150 the subscripts m for model and o for observation (TPXO8-atlas). We therefore obtain the horizontal distributions of $RMSE$
151 for four tidal constituents (see Figs. 2a – 2d). In most model domain, $RMSE$ is less than 0.02 m s^{-1} , but slightly larger in the



152 shallow water (e.g., Luzon Strait and the continental shelf), which is still less than 0.2 m s^{-1} . It may be because that the
153 bathymetry derived from the GEBCO dataset and resolutions in our model differ from those in the TPXO8-atlas, thereby
154 resulting in the discrepancy.

155 In addition to comparison between this model and the global tide model, we extract the DS station outputs with a high
156 sampling rate for comparing with the in-situ observations. To avoid the effects of massive high-frequency motions (i.e.,
157 environmental noises) in the observational time series on the barotropic regime, we first do the harmonic analysis for zonal
158 barotropic velocities from 5 August to 19 September, then extract the amplitude and phase of eight key tidal constituents, and
159 restructure the time series (see red line in Fig. 2e). In terms of the model results, we obtain the time series at station DS in the
160 same way (see black line in Fig. 2e). It is worth mentioning that the discrepancy between the eight-harmonic restructured time
161 series and the raw data in the model is small, since the experiment is basically driven by the eight tidal constituents and does
162 not include any affects from the background environment. By comparing the two timeseries, the model reliability is validated
163 all through the spring and neap tides. Overall, the model presents nice performance in the barotropic regime.

164 3.2 Comparison with MODIS images

165 Apart from the model validation in barotropic tides, we then look over the control run (*500m_8HARs*) in baroclinic (ISWs)
166 regime by comparing the model results with MODIS images. Figs. 3a and 3b both show two successive ISWs (labeled as IW1
167 and IW2) in the deep basin with a distance of $\sim 120 \text{ km}$. The lengths, curvatures and locations of IW1 and IW2 in the simulation
168 are consistent with those in the MODIS image. However, two other ISWs occurring over the continental slope and shelf are
169 captured in the numerical simulations, but not observed on 14 August in the MODIS-Aqua image due to the cloud covering
170 (Fig. 3b). Conversely, the cloud disappeared on 15 August, so the MODIS-Terra sensor gives a clear seascape painting of
171 ISWs both in the shallow water (i.e., IW2) and deep water (i.e., IW3 and IW4). Note that IW2 in Figs. 3b and 3d are the same
172 ISW, which propagates $\sim 250 \text{ km}$ within 19 hours and 35 mins. All ISWs (IW2, IW3 and IW4) in Figs. 3c and 3d occur at the
173 fairly close locations with analogous wave properties. From the perspective of crestline lengths, the numerical model shows
174 well agreement with the MODIS images, namely 131 km versus 133 km for IW2 in Figs. 3a and 3b; 187 km versus 198 km
175 for IW3 and 74 km versus 69 km for IW4 in Figs. 3c and 3d. Besides, in the water depth shallower than 500 m, the modelled
176 IW2 exhibits an ISW train with trailing waves, which is also shown in the MODIS image. As the model neglects wind above
177 the sea surface and other marine dynamical processes, there are still some subtle nuances of wave characteristics between them.
178 Overall, this model nicely demonstrates spatial distributions of ISWs in the NSCS, based on the comparison with remote
179 sensing imagery.

180 3.3 Comparison with in-situ observations

181 To further evaluate the model performance in reproducing ISWs, we introduce the in-situ observations. The vertical structure
182 and timing of the wave arrivals, after crossing the deep basin, can be seen in details using daily plots (Figs. 4a – 4g) of the
183 temperature isotherms and baroclinic (ISW-induced) velocities from 8 to 14 August at mooring DS. For clarity, only the results



184 in upper 900 m are shown in Fig. 4, including the main wave-induced temperature fluctuations. Alford et al. (2010) suggested
185 that the nonlinear internal wave speeds varied from 2.0 m s⁻¹ near the Luzon Strait to 3.0 m s⁻¹ in the deep basin in the NSCS,
186 so it takes roughly two days for ISWs to propagate from the generation site to the targeted station (DS). We move the arrival
187 time (i.e., 8 to 14 August) of ISWs two days forward at the station DS, so the related barotropic tides gradually increase during
188 the spring tidal cycle at the Luzon Strait (i.e., 6 to 12 August). It explains why ISWs were relatively weak and linear from 8 to
189 10 August (Figs. 4a – 4c), but became significant and nonlinear from 11 to 14 August (Figs. 4d – 4g). A single ISW was
190 captured around 12:00 UTC from 11 to 14 August, which arrived at the location at approximately the same time every day
191 (termed as type-a ISWs by Ramp et al. (2004)). Meanwhile, a wave train, consisted of two dominant solitons and some small
192 trailing waves, arrived at the station an hour later each day, showing the same wave characteristics as type-b ISWs in Ramp et
193 al. (2004).

194 In terms of the model, we also use the daily plots (Figs. 4h – 4n) at station DS with 1 min sampling rate to show its similarity
195 to the in-situ observations. An increasing trend of wave amplitude and nonlinearity is obvious from 8 August to 14 August in
196 the model results, suggesting precise depictions of barotropic tides and ISWs' characteristics. Specifically, both type-a (single
197 solitons) and type-b ISWs (wave trains) are displayed with analogous arrival time, wave-induced (baroclinic) velocity (color
198 shades in Fig. 4) and wave amplitude (contours in Fig. 4) to those in the observations. It's worth noting that even the linear
199 internal tides and/ or hydraulic jumps around 12:00 UTC from 8 to 10 August are reproduced. Although the model omits some
200 small wave signals (see blue arrows in Fig. 4e) in the observations, which might be induced by non-tidal processes such as
201 background currents, the model still shows a well performance in the ISW reproduction.

202 To quantitatively identify the model accuracy, we select fifteen ISWs (marked as red arrows in the left column of Fig. 4),
203 extract their wave properties (i.e., arrival time, maximum wave-induced velocity, propagation direction and maximum mode-
204 1 wave amplitude) and compare them between in-situ observations and numerical simulations. In terms of wave propagation
205 direction, we obtain by computing the angle of baroclinic zonal and meridional components in the layer with maximum velocity.
206 The maximum mode-1 wave amplitude (A_1) is extracted from the mooring data and model outputs by least squares fitting
207 density perturbation profiles $\rho'(z)$ to normalized modal structure function $W_n(z)$, following the similar procedures to those
208 described by Buijsman et al. (2010) and Rayson et al. (2012). Although the mode-1 wave amplitude can also be extracted by
209 least squares fitting the horizontal baroclinic velocity, Rayson et al. (2019) suggested that the method in velocity field was
210 fuzzy with unidirectional internal waves. The modal structure function can be resolved by a shear-free Taylor-Goldstein
211 equation with the background stratification $N^2(z)$, which is given by

$$212 \quad \frac{d^2 W_n(z)}{dz^2} + \frac{N^2(z)}{c_n} W_n(z) = 0, \quad (2)$$

213 with the boundary conditions $W_n(0) = W_n(-H) = 0$. Subscript n represents the mode number and c_n is the phase speed of
214 the linear internal waves in n^{th} mode. The buoyancy perturbation $b(z)$, depending on density perturbation $\rho'(z)$, is written as

$$215 \quad b(z) = -g \frac{\rho'(z)}{\rho_0}, \quad (3)$$



216 in which, ρ_0 is the reference density. Following the internal wave polarization relationships (Gerkema and Zimmerman,
217 2008), we fit the wave amplitudes (A_n) in different vertical modes to $b(z)$ in both in-situ observations and numerical
218 simulations via

$$219 \quad b(z) = \sum_{n=1}^5 A_n N^2(z) W_n(z), \quad (4)$$

220 Here, we select the first five vertical modes ($n = 1 - 5$) to do the least squares fitting and mainly discuss the mode-1 wave
221 amplitude (A_1) due to its significant dominance (Fig. 4).

222 According to the above approaches, we extract the four wave properties for fifteen ISWs and plot Fig. 5, in which
223 observation and model results are shown in red and green, respectively. First, we list the arrival time of ISWs on the two sides
224 of Fig. 5. The bias between observation and model is always smaller than 1.5 h and the root mean square deviation (RMSD)
225 is 0.71 h, indicating accurate depiction of ISW arrival time in the control run (*500m_8HARs*). Second, the maximum baroclinic
226 velocity (Fig. 5a) and the averaged values (0.98 m s^{-1} and 1.18 m s^{-1} , respectively) are shown in the solid lines. It is suggested
227 that the model underestimates the baroclinic velocity due to neglect of some background non-tidal signals, thereby introducing
228 a RMSD of 0.41 m s^{-1} . Third, the averaged propagation directions of ISWs are $\sim 285^\circ$ and $\sim 291^\circ$, respectively
229 (the angle measured counterclockwise from north) in the model results and observational data with a RMSD of 8.35° . It is
230 worth mentioning that the type-a ISWs mainly propagate westward while the type-b ISWs propagate north-westward in both
231 observation and model, verifying the model's reliability to some extent. Finally, the averaged maximum mode-1 wave
232 amplitude ($\sim 108 \text{ m}$) in the model is close to that ($\sim 99 \text{ m}$) in the observation. Nonetheless, the RMSD of mode-1 wave amplitude
233 is 37.27 m. Overall, the control run can basically reproduce various wave properties of ISWs observed in the vicinity of the
234 Dongsha Atoll in the NSCS.

235 **4 Assessment of factors affecting three-dimensional model forecasting precision**

236 In this section, based on the control run, we alter the model configurations, such as the requirements of horizontal resolutions,
237 numbers of tidal constituents and initial stratification, to respectively estimate their effects on the model forecasting precision
238 of ISWs in the NSCS.

239 To determine the roles of model horizontal resolutions, tidal constituents and initial stratification in reproducing ISWs in
240 the NSCS, a set of 3D sensitivity numerical simulations are employed with different configurations, which are listed in Table
241 2. Details in configuration changes are as follows.

242 1) Exps. 3 and 4 (*250m_8HARs* and *1000m_8HARs*): Comparing to *500m_8HARs*, the horizontal resolution (Δx) is set as
243 250 m and 1000 m in both zonal and meridional directions, respectively.

244 2) Exps. 5 - 7 (*500m_1HAR*, *500m_4HARs*, and *500m_13HARs*): Comparing to *500m_8HARs*, the sensitivity experiments
245 are driven by single tidal constituent (M2), four main tidal constituents (M2, S2, K1, and O1), and thirteen tidal constituents
246 (M2, S2, N2, K2, K1, O1, P1, Q1, M4, MS4, MN4, MM, and MF), respectively.



247 3) Exp. 8 (*500m_Real_N2*): A real stratification profile of background temperature at the mooring station DS is imposed as
248 the initial condition, which is derived from the in-situ measurements. A backward-in-time low-pass filter derived from a finite
249 impulse response differential equation is used to compute the background temperature (Rayson et al., 2019).

$$250 \quad \frac{d\bar{T}}{dt} = \frac{1}{\tau_f} (T - \bar{T}), \quad (5)$$

251 in which, τ_f is the filtering time scale, set to 35 h, corresponding to the local Coriolis frequency. T and \bar{T} are the
252 instantaneous and background temperature, respectively. Then, the background temperature at each observational time step i
253 is given as

$$254 \quad \bar{T}^{i+1} = \bar{T}^i + \frac{\Delta t}{\tau_f} (T^{i+1} - \bar{T}^i), \quad (6)$$

255 where Δt is the sampling rate (10 secs for the temperature and CTD sensors, 15 secs for the CT sensors). The background
256 temperature profile is ultimately obtained by low-pass filtering at each layer (see red line in Fig. 1b).

257 **4.1 Requirements of resolutions**

258 Various 3D model with different resolutions were implemented to simulate ISWs in the NSCS in previous studies (e.g.,
259 Vlasenko et al., 2010; Zhang et al., 2011; Lai et al., 2019). However, which resolution is adequate to satisfy the ISW prediction
260 precision and save computational resources to the utmost in the meantime has yet been discussed. Here, we run two sensitivity
261 experiments (Exps. *250m_8HARs* and *1000m_8HARs*) with horizontal resolutions of 250 m and 1000 m, to respectively
262 compare the model performance in different aspects with the control run (resolution of 500 m).

263 First, the spatial distributions of ISWs are exhibited via the snapshots of sea surface height gradients ($|\nabla\eta|$) at 12:00 UTC
264 on 12 August 2014. In the control run (*500m_8HARs*), three ISWs (labelled as IWB1, IWA1, and IWB2 from west to east)
265 with distinct crest lines successively occur between 116°E and 120°E (see Fig. 6a), in which IWB1 and IWB2 are internal
266 wave packets with trailing waves (type-b wave) and IWA1 is a single soliton (type-a wave). As IWB1 approaches the
267 continental slope and shelf, the leading wave front fully steepens with a narrow characteristic half-width, suggesting its strong
268 nonlinearity. IWB2 also shows up as a wave packet with many secondary waves in the developing stage, although its
269 nonlinearity is slightly weaker than IWB1's. Conversely, the single soliton IWA1 with relatively long crest line and broad
270 characteristic half-width is about to pass mooring station DS (marked as green star in Fig. 6). In comparison, the Exps.
271 *250m_8HARs* and *1000m_8HARs* reproduce these three waves as well, but with some subtle discrepancies between them. In
272 Exp. *250m_8HARs*, more details of wave properties are clarified (Fig. 6b). Specifically, the secondary waves of IWB1 and
273 IWB2 are more visible than those in *500m_8HARs*. However, in Exp. *1000m_8HARs*, some fine structures of ISWs are not
274 well resolved. For instance, only one secondary wave is found behind the leading wave of IWB2, and the south portion of
275 IWA1 crest line is barely observed (Fig. 6c).

276 Then, we select a transect along the main propagation path of ISWs (shown in dashed line in Fig. 6a) at 12:00 UTC on 12
277 August 2014 to compare the vertical structure of ISWs among three experiments (see Fig. 7). In Fig. 7, blue (yellow) color



278 shades represent westward (eastward) baroclinic velocity and contours are temperature isotherms. Linear internal waves, such
279 as internal wave beams near the generation site ($120^{\circ} - 121^{\circ}\text{E}$), are nicely reproduced in all numerical experiments. Nonetheless,
280 nonlinear internal waves present different wave characteristics in different cases. In Exp. *500m_8HARs*, the single soliton
281 IWA1 and the wave packet IWB2 with a series of trailing waves are apparent in the slice, but IWB1 is not included (Fig. 7a).
282 In Exp. *250m_8HARs*, IWA1 and IWB2 occur at the same location as those in Exp. *500m_8HARs*. IWA1 show similar
283 properties in two cases, but the secondary waves of IWB2 are better described in Exp. *250m_8HARs*. By comparison, IWA1
284 shows its weak nonlinearity with small vertical displacement and broad characteristic half-width (i.e., horizontal distance
285 between the wave front and wave trough) in Exp. *1000m_8HARs*. Besides, only one secondary wave appears in the IWB2
286 packet in Exp. *1000m_8HARs*.

287 Last, a two-day time segment of observational temperature and baroclinic velocities from 18:00 UTC 11 August to 18:00
288 UTC 13 August 2014 at the station DS is extracted to demonstrate the sensitivity model capability of simulating vertical
289 structures of ISWs over the continental slope (Fig. 8). In the control run (*500m_8HARs*, Fig. 8b), two wave packets and two
290 single solitons successively arrive at the station, keeping the consistency with the observation, although their characteristic
291 half-widths are slightly broader than those in the field measurements (Fig. 8a). Meanwhile, some small fluctuations, occurring
292 in the observations, are not included in the control run. In Exp. *250m_8HARs* (Fig. 8c), the half-widths are narrower than
293 those in the Exp. *500m_8HARs*, which agree better with the real internal wave field. Besides, more fluctuations, i.e., those
294 small wave signals (09:00 UTC 12 August and 09:00 UTC 13 August) in front of the single solitons are reproduced in this
295 experiment. Conversely, in Exp. *1000m_8HARs*, internal wave trains can still be reproduced with relatively weak nonlinearity,
296 but the single solitons are not correct due to their tiny amplitudes and linear wave structures.

297 To quantitatively evaluate the model performance of sensitivity experiments, we present the bias of five wave properties of
298 fifteen ISWs (marked as red arrows in Fig. 4) between model results and observational data in Fig. 9. The biases of arrival
299 time are generally smaller than 1 h (see black and blue circles in Fig. 9a) for Exps. *500m_8HARs* and *250m_8HARs*, whose
300 RMSDs are 0.71 and 0.67 h, respectively. In contrast, the bias for Exp. *1000m_8HARs* is larger than 1 h (red circles in Fig.
301 9a) and its RMSD is 0.79 h. In terms of the wave-induced velocity (Fig. 9b), the RMSDs are 0.38, 0.41 and 0.48 m s^{-1} in Exps.
302 *250m_8HARs*, *500m_8HARs*, and *1000m_8HARs*, respectively. The RMSDs of propagation directions are very close ($\sim 8.5^{\circ}$)
303 in the three experiments (see Table 3). As for the mode-1 wave amplitudes, Exps. *250m_8HARs* and *500m_8HARs*
304 overestimate the wave amplitudes in most cases (see positive biases in Fig. 9d), thereby resulting in RMSDs of 38.12 and
305 37.27 m, respectively. Conversely, Exp. *1000m_8HARs* would underestimate the wave amplitudes of majority ISWs with
306 dominant negative biases in Fig. 9d, resulting in a RMSD of 40.28 m (Table 3). Last but not least, Exps. *500m_8HARs* and
307 *1000m_8HARs* inaccurately depict characteristic half-widths of ISWs with RMSDs of 1.07 and 2.41 km, while Exp.
308 *250m_8HARs* performs well with a RMSD of 0.64 km (Fig. 9e). The relative difference of RMSD suggests that Exp.
309 *250m_8HARs* increases 40% accuracy of predicting characteristic half-widths by comparing to Exp. *500m_8HARs*. From the
310 perspective of computational resources, Exps. *250m_8HARs*, *500m_8HARs*, and *1000m_8HARs* spend 20.4×10^4 CPU
311 hours, 4.6×10^4 CPU hours, and 1.0×10^4 CPU hours, respectively.



312 In summary, the control run with a resolution of 500 m can basically reproduce the principal ISW field in the NSCS, while
313 the sensitivity model with a higher resolution of 250 m would be a better solution to identify wave properties, in particular of
314 the wave nonlinearity. Nonetheless, a 250 m-resolution model spends nearly fivefold computational resources of a 500 m-
315 resolution model in the same model domain. Besides, the model with a lower resolution of 1000 m underestimates the
316 nonlinearity of ISWs, thereby resulting in an inaccurate ISW field in the NSCS.

317 **4.2 Requirements of tidal constituents**

318 3D/2D models with different numbers of barotropic tidal constituents (e.g., single harmonic, four harmonics and eight
319 harmonics) were commonly imposed to investigate the generation mechanisms of ISWs in the NSCS in previous studies (e.g.,
320 Li, 2014; Buijsman et al., 2010; Jin et al., 2021). However, whether a single tidal constituent can satisfy the reproduction of a
321 real ISW field and how many tidal constituents are required for a realistic ISW model are still questions. Here, we run three
322 sensitivity experiments (Exps. *500m_1HAR*, *500m_4HARs* and *500m_13HARs*) with different numbers of tidal harmonics to
323 answer the questions by comparing the model performance with the control run (*500m_8HARs*).

324 We first discuss the model requirements of tidal constituents from the point of view of the ISW horizontal distributions and
325 look back to Fig. 6. Note that time series of zonal barotropic currents at the generation site (Luzon Strait) are presented on the
326 bottom left for each panel, where single/four/eight tidal constituent(s) are shown in green/magenta/blue. By comparing Exp.
327 *500m_1HAR* (Fig. 6d) and *500m_8HARs* (Fig. 6a), we find that the single M2 tidal harmonic is not adequate to reproduce
328 ISWs in the NSCS, so only some linear internal tides are detected on the sea surface via $|\nabla\eta|$. In contrast, Exp. *500m_4HARs*
329 (Fig. 6e) nearly recreates the analogous scenario of ISWs to Exp. *500m_8HARs*, where IWB1, IWA1 and IWB2 appear at the
330 same locations. Nonetheless, the crestline length (~134 km) of IWB2 in Exp. *500m_4HARs* is slightly shorter than that (~167
331 km) in Exp. *500m_8HARs*, and the secondary waves of IWB2 are unclear in Exp. *500m_4HARs* (see Fig. 6e). $|\nabla\eta|$ in Exp.
332 *500m_13HARs* are not presented in Fig. 6, since it shows the exact same spatial patterns of ISWs as those in Exp.
333 *500m_8HARs*, suggesting the principle eight tidal constituents are fine enough to satisfy accurate reproduction of the
334 horizontal features of ISWs in a realistic oceanic model.

335 We then consider the difference of ISW vertical structures in sensitivity experiments with various tidal forcing via the
336 selected transect and mooring station DS. In Exp. *500m_1HAR*, only linear internal waves are captured from the generation
337 site to the slope, suggesting that single M2 tidal constituent without amplification factors can only contributes to internal tides
338 and linear internal wave beams in NSCS (see Figs. 7d and 8e), unless the magnitudes of M2 barotropic tides are amplified,
339 ISWs are likely to be generated (e.g., Yuan et al., 2020). In Exp. *500m_4HARs* (Figs. 7e and 8f), the single soliton IWA1 is
340 reproduced with a smaller amplitude and weaker nonlinearity than that in Exp. *500m_8HARs*. Besides, the secondary waves
341 of IWB2 are barely observed in Exp. *500m_4HARs*, which are much clearer in Exp. *500m_8HARs* (Figs. 7a and 8a). Figs. 8a
342 and 8g depict the striking similarity of wave characteristics between Exp. *500m_8HARs* and Exp. *500m_13HARs*.

343 Last, we quantitatively estimate the sensitivity model capability of reproducing ISWs, by computing the biases and RMSDs
344 of five wave properties (see Fig. 9 and Table 3) in the cases with different tidal forcing. Since Exp. *500m_1HAR* cannot predict



345 ISWs with significant amplitudes, we exclude it in the following analysis. In terms of Exp. *500m_13HARs* with thirteen tidal
346 constituents, the biases and RMSDs of five wave properties are very close to those in the control run with eight harmonics (see
347 overlapped black and cyan circles in Fig. 9 and Table 3). Conversely, Exp. *500m_4HARs* shows significant difference in the
348 biases and RMSDs of five wave properties from the control run. Specifically, in Fig. 9a, the RMSD of arrival time (0.81 h) is
349 larger in Exp. *500m_4HARs* than that in Exp. *500m_8HARs* (0.71 h). In addition, Exp. *500m_4HARs* underestimates averaged
350 wave-induced velocity for about 38% and averaged mode-1 wave amplitude for about 15%, which result in large negative
351 values of biases (see magenta circles in Figs. 9b and 9c), corresponding to 0.58 m s^{-1} and 43.69 m of RMSDs, respectively. In
352 terms of the characteristic half-widths, Exps. *500m_4HARs* and *500m_13HARs* with RMSDs of 1.10 and 1.01 km show
353 analogous performance to the control run Exp. *500m_8HARs* with a RMSD of 1.07 km.

354 In summary, the model with eight (or thirteen) primary tidal constituents can accurately reproduce the real ISW field in the
355 NSCS, while the sensitivity model with four key harmonics (M2, S2, K1 and O1) would underestimate the magnitudes of
356 some secondary wave within a wave packet. In addition, the model only driven by M2 tide can only characterize wave
357 properties of linear internal waves (tides) instead of ISWs.

358 **4.3 Initial stratification selections**

359 As ISWs generate via tide-topography interaction in the stratified water, the stratification selection is crucial to directly
360 affect the model capabilities. Here, we extract the background stratification from the in-situ measurements at mooring station
361 DS as initial condition to run the sensitivity experiment *500m_Real_N2*, and compare the model results with the control run
362 (*500m_8HARs*) with a climatological stratification from the WOA18 dataset.

363 In the model results, the spatial distribution of $|\nabla\eta|$ in Exp. *500m_Real_N2* shows analogous pattern of ISWs to that in Exp.
364 *500m_8HARs*. Specifically, three ISWs (i.e., IWB1, IWA1, and IWB2) appear at the same location in the two experiments
365 with similar horizontal wave characteristics (Figs. 6a and 6f). The visible difference is that the crest line length of the secondary
366 wave of IWB2 is longer with a stronger nonlinearity in Exp. *500m_Real_N2*. We then look over the difference of ISW vertical
367 structures between two cases from the perspective of x - z plane along the transect (Figs. 7a and 7f) and time series at station
368 DS (Figs. 8a and 8h). It is clearly shown that Exp. *500m_Real_N2* with the real stratification can better characterize the
369 nonlinearity of the single soliton IWA1 and the secondary wave of wave train IWB2. Besides, the comparison with field
370 measurements reveals that Exp. *500m_Real_N2* shows a better precision (13%) in predicting the arrival time (i.e., RMSD of
371 0.62 h) of ISWs than the control run (i.e., RMSD of 0.71 h) with the climatological stratification. However, the RMSD of the
372 propagation direction of ISWs is larger in the realistic-stratification case (14.74°) than that of the control run (8.35°). Last, Exp.
373 *500m_Real_N2* nicely describes the characteristic half-widths of ISWs (RMSD of 0.58 km), which improves 46% accuracy
374 by comparing that in Exp. *500m_8HARs* (RMSD of 1.07 km). To sum up, although the model with climatological stratification
375 works well, applying the real background stratification as the model initial condition would improve the model performance
376 in predicting some wave properties, including arrival time, wave-induced velocity, wave amplitude and characteristic half-
377 width.



378 5 Discussion and Conclusions

379 Although the three-dimensional realistic model, particularly in Exp. *250m_8HARs*, has accurately reproduced the ISW
380 features in the NSCS to some extent, the depictions of soliton numbers within an internal wave packet and propagation
381 direction still have space for improvement, i.e., at least three following factors might be considered in the future modelling.

382 The first factor, that may affect the model accuracy, is background currents. Here, we download the HYCOM dataset in
383 2014 and calculate the background current field by averaging from 05-AUG to 20-AUG, namely predicting time of the model
384 (see Fig. 10a). In Fig. 10a, there is a clear counter-clockwise circulation/eddy pattern on the west side of Luzon Strait. Xie et
385 al. (2015) suggested that wave properties of ISWs can be significantly influenced by an isolated mesoscale eddy, regardless of
386 a cyclonic or anticyclonic eddy, during the propagation of ISWs. When an ISW pass over a cyclonic eddy, as in Fig. 10a, the
387 crestline will be distorted, thereby modulating the oblique propagation direction of wave to some extent (Xie et al., 2016). In
388 addition, a series of secondary trailing waves are able to form behind the leading wave in the energy-focusing region. Therefore,
389 background currents are supposed to be considered in the future forecasting model, which shows potential improvement in the
390 depiction of soliton numbers within an ISW packet and propagation direction in the NSCS.

391 The second factor is inhomogeneous spatial distribution of stratification. In the current forecasting model, we apply
392 horizontally-homogeneous temperature and salinity profiles (Fig. 1d) with the maximum buoyancy frequency of $\sim 0.02 \text{ s}^{-1}$ at a
393 water depth of 50 m. However, the stratification is spatially varying in the real ocean (see Fig. 10b, time-averaged buoyancy
394 frequency derived from the HYCOM dataset), although buoyancy frequency is ranging from 0.015 to 0.025 s^{-1} in the most
395 model region. Since wave speeds of ISWs and internal tides are closely related to vertical structure of stratification based on
396 eigen-function, the inhomogeneous stratification pattern is likely to affect ISW propagation speed and then modulate their
397 arrival time. Most of previous numerical studies (e.g., Zhang et al., 2011; Alford et al., 2015; Zeng et al., 2019) rarely
398 considered the impacts of horizontally inhomogeneous stratification, but Chi et al. (2016) and Lai et al. (2019) applied spatially
399 varying stratification in 3D model and indicated that inhomogeneous stratification can achieve better model results to some
400 extent. Hence, spatially varying stratification is worthwhile to be considered in future numerical studies in the NSCS.

401 The last element is external (wind) forcing. As is well known, internal waves are a ubiquitous phenomenon, of which
402 maximum amplitudes happen in the ocean interior. Nonetheless, the thermoclines usually occur in the upper layers (shallower
403 than 500 m) in the SCS, which can be significantly affected by extreme wind events (i.e., tropical cyclones, Zhang 2022). So
404 far, wind forcing was rarely applied in the numerical modelling of ISWs, except Lai et al. (2019). As both the ISWs and
405 tropical cyclones are active and frequent in August, September and October in the SCS, the impacts of tropical cyclones on
406 the upper layers should be considered in the future numerical simulations, although tropical cyclone does not happen during
407 our predicting period (see Fig. 10c).

408 In summary, this study introduces a robust ISW forecasting model by comparing with in-situ observational data and remote-
409 sensing images, and quantitatively evaluates the requirements of different factors, including the horizontal resolutions, tidal



410 constituents and initial stratification, for accurately characterizing the ISW field with applications to the NSCS. The major
411 findings are listed as follows.

- 412 1) A model with a 500 m resolution can basically reproduce the principal ISW field, while a model with a higher resolution
413 of 250 m would be a better solution to identify wave properties but spends nearly fivefold computational resources of
414 a 500 m-resolution case with the same model domain.
- 415 2) At least eight primary tidal constituents should be included in the boundary forcing.
- 416 3) Compared to climatological stratification, applying the observational background stratification could improve the
417 model performance in predicting some wave properties, namely 13% improvement of arrival time and 46%
418 improvement of characteristic half-width.

419 **Appendix A: Feasibility study of two-dimensional slice model**

420 Differing from the 3D models, 2D slice models are fairly economical from the perspective of computational resources. In
421 the past few decades, 2D slice models with idealized topography (double ridges) were commonly conducted to investigate
422 ISW dynamics in the NSCS, in particular for the generation mechanisms and the affecting factors of ISWs (i.e., Cai et al.,
423 2002; Shaw et al., 2009; Li, 2014). Here, we attempt to test the 2D model performance along different transects and clarify
424 whether a 2D slice model can be a substitute for a 3D model in the aspect of reproducing a real ISW field in the NSCS.

425 Three parallel transects with a distance of 0.05° are selected along the main propagation direction of ISWs (see dashed lines
426 in Fig. 1a), which are labelled as *2D_500m_8HARs*, *2D_500m_8HARs_005N*, and *2D_500m_8HARs_005S*. Δx and Δt are
427 still set as 500 m and 10 sec, respectively. Initial conditions and dissipation coefficients are set the same as those in the 3D
428 control run (*500m_8HARs*). The 2D slice models are also driven by the barotropic tides of eight tidal constituents at both west
429 boundary (115.8°E , $21.1^\circ\text{N} \pm 0.05^\circ$) and east boundary (123.8°E , $19.5^\circ\text{N} \pm 0.05^\circ$). As the transects are not strictly zonal (angle
430 $\theta = 11.2^\circ$, see Fig. 1a), it is necessary to extract the amplitude (U') and phase (ϕ') for each harmonic (ω) in the transect
431 direction from the TPX08-atlas dataset (i.e., U , V , ϕ_U , and ϕ_V), given by

432

$$433 \quad U' = \sqrt{(U \cdot \cos\phi_U \cos\theta - V \cdot \cos\phi_V \sin\theta)^2 + (U \cdot \sin\phi_U \cos\theta - V \cdot \sin\phi_V \sin\theta)^2}, \quad (A1)$$

$$434 \quad \phi' = \arctan\left(\frac{U \cdot \sin\phi_U \cos\theta - V \cdot \sin\phi_V \sin\theta}{U \cdot \cos\phi_U \cos\theta - V \cdot \cos\phi_V \sin\theta}\right), \quad (A2)$$

435 Here, we apply the standard 2D experiment along the selected transect (see the black dashed line in Fig. 1a) and label it as
436 *2D_500m_8HARs*. The model is driven by eight principle tidal constituents on the both lateral boundaries, which are extracted
437 from the TPX08 dataset (following Eqns. A1 and A2). Note that initial conditions and other model configurations in Exp.
438 *2D_500m_8HARs* are the same as those in the 3D control run (*500m_8HARs*). In addition, we run two sensitivity experiments
439 (Exps. *2D_500m_8HARs_005N* and *2D_500m_8HARs_005S*) along the two parallel transects (see red dashed lines in Fig.
440 1b).



441 In the 2D standard case (*2D_500m_8HARs*), ISWs subsequently generate in the double ridge, then propagate westward,
442 and eventually arrive at the station in the form of wave trains (Fig. A1b). The wave amplitudes are greater than those in the
443 3D control run (Fig. A1a). At the station outputs (Fig. A1f), we find that Exp. *2D_500m_8HARs* can only reproduce ISW
444 packets, but cannot discriminate type-a and type-b ISWs. Although the occurrence frequency of ISWs is also twice per day in
445 Exp. *2D_500m_8HARs*, the arrival time of those ISW packets is not consistent with that in Exp. *500m_8HARs* (Fig. A1e) and
446 in the field measurements (Fig. 8a). In Exp. *2D_500m_8HARs_005N*, ISWs are rarely found along the transect (Fig. A1c),
447 likely due to the relatively gentle topography and small tidal forcing at the lateral boundaries. At the station outputs (Fig. A1g),
448 only small temperature fluctuations are captured. Conversely, Exp. *2D_500m_8HARs_005S* show analogous wave fields to
449 Exp. *2D_500m_8HARs* (Fig. A1d). Specifically, ISW packets with a half-day cycle are dominant, but their arrival time are
450 postponed for about two hours (Fig. A1h).

451 To sum up, 2D slice models along different transects (even 0.05° apart) present totally different ISW characteristics, which
452 are inconsistent with the 3D model results and in-situ measurements. Therefore, 3D model is the best and sole option to
453 correctly reproduce the ISW field in the real ocean, while 2D model is more suitable for the mechanism investigations.

454

455 *Code and data availability.* The MODIS remote-sensing images are derived from the NASA Worldview application
456 (<https://worldview.earthdata.nasa.gov>). The Massachusetts Institute of Technology general circulation model used for
457 simulating nonlinear internal waves is available at <https://mitgcm.org/source-code/> and developed openly at
458 <https://github.com/MITgcm/MITgcm/commits/master>. The input files (including initial and boundary conditions) and relevant
459 output data files of the three-dimensional realistic model in the northern South China Sea are available at a free, open access,
460 data repository via <https://doi.org/10.5281/zenodo.6792999>. The field observational data at the Dongsha mooring station is
461 available at the repository via <https://doi.org/10.5281/zenodo.6793125>.

462

463 *Author contributions.* YG wrote the paper with the help of all the co-authors. XC, JX, JX, ZC, YH and SC provided constructive
464 feedback on the manuscript. JX gave help and advice in observational data processing and numerical simulations.

465

466 *Competing interests.* The authors declare that they have no conflict of interest.

467

468 *Financial support.* This work was jointly supported by the National Natural Science Foundation of China (NSFC) under
469 contract Nos. 42130404, 91858201, 42206012, 42276015, 42276022 and 42176025; the Key Research Program of Frontier
470 Sciences, Chinese Academy of Sciences (CAS) under contract No. QYZDJ-SSW-DQC034; the China Postdoctoral Science
471 Foundation (2022M713232); Grant No. ISEE2021PY01 from CAS; Youth science and technology innovation talent of
472 Guangdong TeZhi plan (2019TQ05H519); Rising Star Foundation of SCSIO (NHXX2019WL0201); Natural Science
473 Foundation of Guangdong Province (2020A1515010495, 2021A1515012538, 2021A1515011613); the Youth Innovation
474 Promotion Association from CAS (2019336); the State Key Laboratory of Tropical Oceanography Independent Research



475 Program under contract No. LTOZZ2205. The numerical simulation is supported by the High Performance Computing
476 Division and HPC managers of Wei Zhou and Dandan Sui in the South China Sea Institute of Oceanology.

477

478 **References**

479 Alford, M. H., MacKinnon, J. A., Nash, J. D., Simmons, H., Pickering, A., Klymak, J. M., Pinkel, R., Sun, O., Rainville, L.,
480 Musgrave, R., Beitzel, T., Fu, K. H., and Lu, C. W.: Energy flux and dissipation in Luzon Strait: Two tales of two
481 ridges. *Journal of Physical Oceanography*, 41, 2211-2222, <https://doi.org/10.1175/JPO-D-11-073.1>, 2011.

482 Alford, M. H., Peacock, T., MacKinnon, J. A., Nash, J. D., Buijsman, M. C., Centurioni, L. R., ... and Paluszkiwicz, T.: The
483 formation and fate of internal waves in the South China Sea, *Nature*, 521, 65-69, <https://doi.org/10.1038/nature14399>, 2015.

484 Álvarez, Ó., Izquierdo, A., González, C. J., Bruno, M., and Mañanes, R.: Some considerations about non-hydrostatic vs.
485 hydrostatic simulation of short-period internal waves. A case study: The Strait of Gibraltar. *Continental Shelf Research*, 181,
486 174-186, <https://doi.org/10.1016/j.csr.2019.05.016>, 2019.

487 Beardsley, R. C., Duda, T. F., Lynch, J. F., Irish, J. D., Ramp, S. R., Chiu, C. S., Tang, T. Y., Yang, Y. J., and Fang, G.:
488 Barotropic tide in the northeast South China Sea, *IEEE Journal of Oceanic Engineering*, 29, 1075-1086,
489 <https://doi.org/10.1109/JOE.2004.833226>, 2004.

490 Buijsman, M. C., Kanarska, Y., and McWilliams, J. C.: On the generation and evolution of nonlinear internal waves in the
491 South China Sea, *Journal of Geophysical Research: Oceans*, 115, <https://doi.org/10.1029/2009JC005275>, 2010.

492 Buijsman, M. C., McWilliams, J. C., and Jackson, C. R.: East-west asymmetry in nonlinear internal waves from Luzon
493 Strait, *Journal of Geophysical Research: Oceans*, 115, <https://doi.org/10.1029/2009JC006004>, 2010.

494 Cai, S., Long, X., and Gan, Z.: A numerical study of the generation and propagation of internal solitary waves in the Luzon
495 Strait, *Oceanologica Acta*, 25, 51-60, [https://doi.org/10.1016/S0399-1784\(02\)01181-7](https://doi.org/10.1016/S0399-1784(02)01181-7), 2002.

496 Chen, Z., Nie, Y., Xie, J., Xu, J., He, Y., and Cai, S.: Generation of internal solitary waves over a large sill: From Knight Inlet
497 to Luzon Strait, *Journal of Geophysical Research: Oceans*, 122, 1555-1573, <https://doi.org/10.1002/2016JC012206>, 2017.

498 Cummins, P. F., and Oey, L. Y.: Simulation of barotropic and baroclinic tides off northern British Columbia, *Journal of*
499 *Physical oceanography*, 27, 762-781, [https://doi.org/10.1175/1520-0485\(1997\)027<0762:SOBABT>2.0.CO;2](https://doi.org/10.1175/1520-0485(1997)027<0762:SOBABT>2.0.CO;2), 1997.

500 Du, T., Tseng, Y. H., and Yan, X. H.: Impacts of tidal currents and Kuroshio intrusion on the generation of nonlinear internal
501 waves in Luzon Strait, *Journal of Geophysical Research: Oceans*, 113, <https://doi.org/10.1029/2007JC004294>, 2008.

502 Egbert, G. D., and Erofeeva, S. Y.: Efficient inverse modeling of barotropic ocean tides, *Journal of Atmospheric and Oceanic*
503 *technology*, 19, 183-204, [https://doi.org/10.1175/1520-0426\(2002\)019<0183:EIMOBO>2.0.CO;2](https://doi.org/10.1175/1520-0426(2002)019<0183:EIMOBO>2.0.CO;2), 2002.

504 Farmer, D., Li, Q., and Park, J. H.: Internal wave observations in the South China Sea: The role of rotation and non-
505 linearity, *Atmosphere-Ocean*, 47, 267-280, <https://doi.org/10.3137/OC313.2009>, 2009.



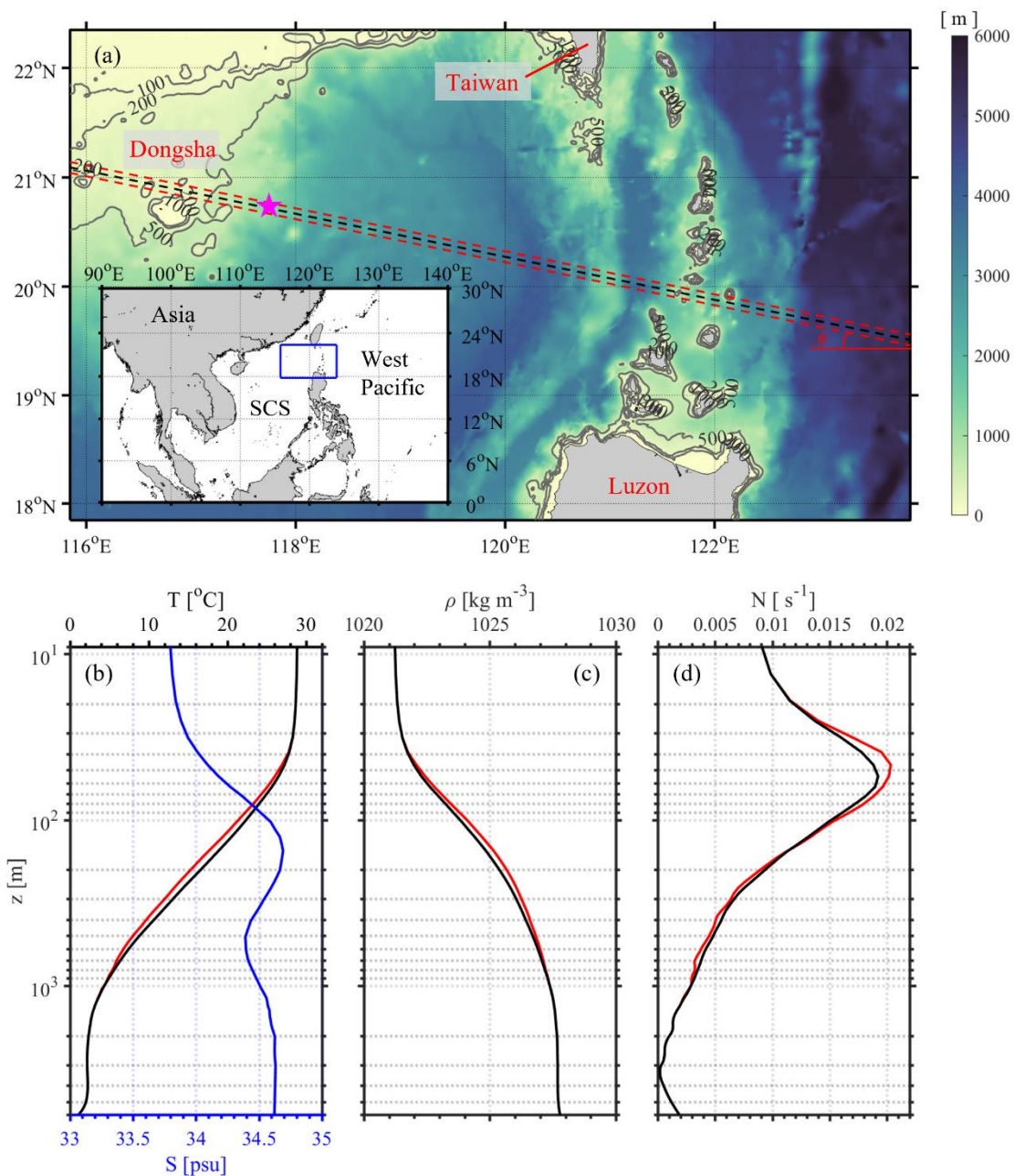
- 506 Farmer, D. M., Alford, M. H., Lien, R. C., Yang, Y. J., Chang, M. H., and Li, Q.: From Luzon Strait to Dongsha Plateau:
507 Stages in the life of an internal wave, *Oceanography*, 24, 64-77, 2011.
- 508 Gerkema, T., and Zimmerman, J. T. F.: An introduction to internal waves, Lecture Notes, Royal NIOZ, Texel, 207, 2008.
- 509 Guo, C., Chen, X., Vlasenko, V., and Stashchuk, N.: Numerical investigation of internal solitary waves from the Luzon Strait:
510 Generation process, mechanism and three-dimensional effects, *Ocean Modelling*, 38, 203-216,
511 <https://doi.org/10.1016/j.ocemod.2011.03.002>, 2011.
- 512 Huang, W., Johannessen, J., Alpers, W., Yang, J., and Gan, X.: Spatial and temporal variations of internal wave sea surface
513 signatures in the northern South China Sea studied by spaceborne SAR imagery, In Proceedings of the 2nd SeaSAR
514 Symposium, 2008.
- 515 Jan, S., Lien, R. C., and Ting, C. H.: Numerical study of baroclinic tides in Luzon Strait. *Journal of Oceanography*, 64, 789-
516 802, <https://doi.org/10.1007/s10872-008-0066-5>, 2008.
- 517 Jin, G., Lai, Z., and Shang, X.: Numerical study on the spatial and temporal characteristics of nonlinear internal wave energy
518 in the Northern South China sea, *Deep Sea Research Part I: Oceanographic Research Papers*, 178, 103640,
519 <https://doi.org/10.1016/j.dsr.2021.103640>, 2021.
- 520 Ko, D. S., Martin, P. J., Rowley, C. D., and Preller, R. H.: A real-time coastal ocean prediction experiment for
521 MREA04. *Journal of Marine Systems*, 69, 17-28, <https://doi.org/10.1016/j.jmarsys.2007.02.022>, 2008.
- 522 Lai, Z., Jin, G., Huang, Y., Chen, H., Shang, X., and Xiong, X.: The generation of nonlinear internal waves in the South China
523 Sea: A three-dimensional, nonhydrostatic numerical study, *Journal of Geophysical Research: Oceans*, 124, 8949-8968,
524 <https://doi.org/10.1029/2019JC015283>, 2019.
- 525 Legg, S., and Huijts, K. M.: Preliminary simulations of internal waves and mixing generated by finite amplitude tidal flow
526 over isolated topography, *Deep Sea Research Part II: Topical Studies in Oceanography*, 53, 140-156,
527 <https://doi.org/10.1016/j.dsr2.2005.09.014>, 2006.
- 528 Li, Q.: Numerical assessment of factors affecting nonlinear internal waves in the South China Sea, *Progress in*
529 *Oceanography*, 121, 24-43, <https://doi.org/10.1016/j.pocean.2013.03.006>, 2014.
- 530 Li, D., Chen, X., and Liu, A.: On the generation and evolution of internal solitary waves in the northwestern South China
531 Sea, *Ocean Modelling*, 40, 105-119, <https://doi.org/10.1016/j.ocemod.2011.08.005>, 2011.
- 532 Liu, A. K., Chang, Y. S., Hsu, M. K., and Liang, N. K.: Evolution of nonlinear internal waves in the East and South China
533 Seas, *Journal of Geophysical Research: Oceans*, 103, 7995-8008, <https://doi.org/10.1029/97JC01918>, 1998.
- 534 Liu, A. K., and Hsu, M. K.: Internal wave study in the South China Sea using synthetic aperture radar (SAR), *International*
535 *Journal of Remote Sensing*, 25, 1261-1264, <https://doi.org/10.1080/01431160310001592148>, 2004.
- 536 Locarnini, M. M., Mishonov, A. V., Baranova, O. K., Boyer, T. P., Zweng, M. M., Garcia, H. E., Reagan, J. R., Seidov, D.,
537 Weathers, K. W., Paver, C. R., and Smolyar, I.: World ocean atlas 2018, volume 1: Temperature, 2018.
- 538 Marshall, J., Hill, C., Perelman, L., and Adcroft, A.: Hydrostatic, quasi-hydrostatic, and nonhydrostatic ocean
539 modelling, *Journal of Geophysical Research: Oceans*, 102, 5733-5752, <https://doi.org/10.1029/96JC02776>, 1997.



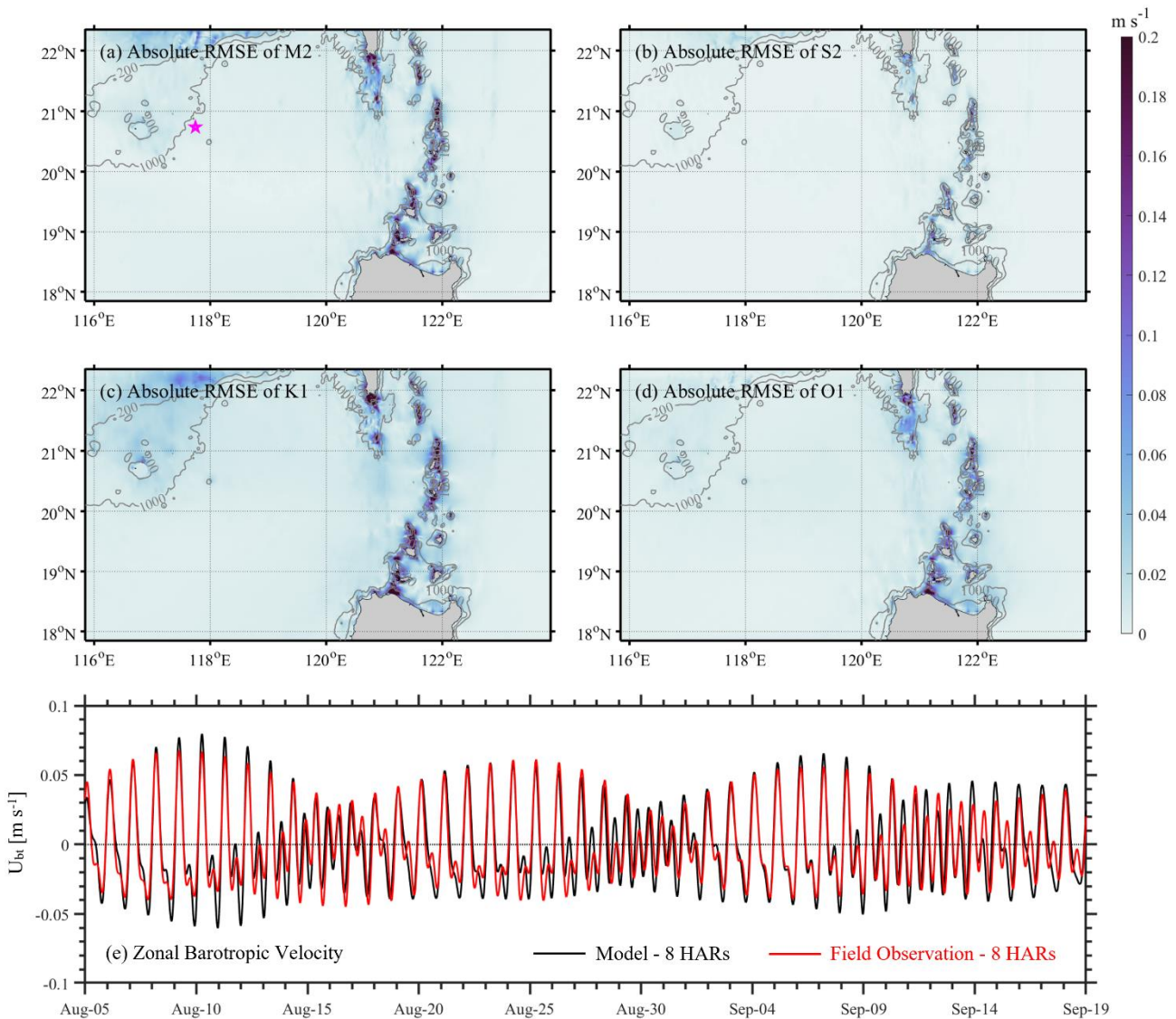
- 540 Orr, M. H., and Mignerey, P. C.: Nonlinear internal waves in the South China Sea: Observation of the conversion of depression
541 internal waves to elevation internal waves, *Journal of Geophysical Research: Oceans*, 108,
542 <https://doi.org/10.1029/2001JC001163>, 2003.
- 543 Nagai, T., and Hibiya, T.: Internal tides and associated vertical mixing in the Indonesian Archipelago. *Journal of Geophysical*
544 *Research: Oceans*, 120, 3373-3390, <https://doi.org/10.1002/2014JC010592>, 2015.
- 545 Ramp, S. R., Tang, T. Y., Duda, T. F., Lynch, J. F., Liu, A. K., Chiu, C. S., Bahr, F. L., Kim, H. R., and Yang, Y. J.: Internal
546 solitons in the northeastern South China Sea, Part I: Sources and deep water propagation. *IEEE Journal of Oceanic*
547 *Engineering*, 29, 1157-1181, 2004.
- 548 Ramp, S. R., Park, J. H., Yang, Y. J., Bahr, F. L., and Jeon, C.: Latitudinal structure of solitons in the South China Sea, *Journal*
549 *of Physical Oceanography*, 49, 1747-1767, <https://doi.org/10.1175/JPO-D-18-0071.1>, 2019.
- 550 Rayson, M. D., Jones, N. L., and Ivey, G. N.: Temporal variability of the standing internal tide in the Browse Basin, Western
551 Australia, *Journal of Geophysical Research: Oceans*, 117, <https://doi.org/10.1029/2011JC007523>, 2012.
- 552 Rayson, M. D., Jones, N. L., and Ivey, G. N.: Observations of large-amplitude mode-2 nonlinear internal waves on the
553 Australian North West shelf, *Journal of Physical Oceanography*, 49, 309-328, <https://doi.org/10.1175/JPO-D-18-0097.1>, 2019.
- 554 Simmons, H., Chang, M. H., Chang, Y. T., Chao, S. Y., Fringer, O., Jackson, C. R., and Ko, D. S.: Modeling and prediction
555 of internal waves in the South China Sea, *Oceanography*, 24, 88-99, 2011.
- 556 Shaw, P. T., Ko, D. S., and Chao, S. Y.: Internal solitary waves induced by flow over a ridge: With applications to the northern
557 South China Sea, *Journal of Geophysical Research: Oceans*, 114, <https://doi.org/10.1029/2008JC005007>, 2009.
- 558 Stewart, K. D., Hogg, A. M., Griffies, S. M., Heerdegen, A. P., Ward, M. L., Spence, P., and England, M. H.: Vertical resolution
559 of baroclinic modes in global ocean models, *Ocean Modelling*, 113, 50-65, <https://doi.org/10.1016/j.ocemod.2017.03.012>,
560 2017.
- 561 Thompson, D. R., and Gasparovic, R. F.: Intensity modulation in SAR images of internal waves, *Nature*, 320, 345-348,
562 <https://doi.org/10.1038/320345a0>, 1986.
- 563 Jackson, C. R., Da Silva, J. C., and Jeans, G.: The generation of nonlinear internal waves, *Oceanography*, 25, 108-123, 2012.
- 564 Vlasenko, V., Stashchuk, N., Guo, C. H. U. N. S. H. E. N. G., and Chen, X.: Multimodal structure of baroclinic tides in the
565 South China Sea, *Nonlinear Processes in Geophysics*, 17, 529-543, <https://doi.org/10.5194/npg-17-529-2010>, 2010.
- 566 Xu, J., He, Y., Chen, Z., Zhan, H., Wu, Y., Xie, J., Shang, X., Ning, D., Fang, W., and Cai, S.: Observations of different effects
567 of an anti-cyclonic eddy on internal solitary waves in the South China Sea, *Progress in Oceanography*, 188, 102422,
568 <https://doi.org/10.1016/j.pocean.2020.102422>, 2020.
- 569 Zeng, Z., Chen, X., Yuan, C., Tang, S., and Chi, L.: A numerical study of generation and propagation of type-a and type-b
570 internal solitary waves in the northern South China Sea, *Acta Oceanologica Sinica*, 38, 20-30, [https://doi.org/10.1007/s13131-
571 019-1495-2](https://doi.org/10.1007/s13131-019-1495-2), 2019.



- 572 Zhang, Z., Fringer, O. B., and Ramp, S. R.: Three-dimensional, nonhydrostatic numerical simulation of nonlinear internal
573 wave generation and propagation in the South China Sea, *Journal of Geophysical Research: Oceans*, 116,
574 <https://doi.org/10.1029/2010JC006424>, 2011.
- 575 Zhang, H.: Modulation of Upper Ocean Vertical Temperature Structure and Heat Content by a Fast-Moving Tropical
576 Cyclone. *Journal of Physical Oceanography*, <https://doi.org/10.1175/JPO-D-22-0132.1>, 2022.
- 577 Zhao, Z., Klemas, V., Zheng, Q., and Yan, X. H.: Remote sensing evidence for baroclinic tide origin of internal solitary waves
578 in the northeastern South China Sea, *Geophysical research letters*, 31, <https://doi.org/10.1029/2003GL019077>, 2004.
- 579 Zhao, Z., and Alford, M. H.: Source and propagation of internal solitary waves in the northeastern South China Sea, *Journal*
580 *of Geophysical Research: Oceans*, 111, <https://doi.org/10.1029/2006JC003644>, 2006.
- 581 Zheng, Q., Yuan, Y., Klemas, V., and Yan, X. H.: Theoretical expression for an ocean internal soliton synthetic aperture radar
582 image and determination of the soliton characteristic half width, *Journal of Geophysical Research: Oceans*, 106, 31415-31423,
583 <https://doi.org/10.1029/2000JC000726>, 2001.
- 584 Zheng, Q., Susanto, R. D., Ho, C. R., Song, Y. T., and Xu, Q.: Statistical and dynamical analyses of generation mechanisms
585 of solitary internal waves in the northern South China Sea, *Journal of Geophysical Research: Oceans*, 112,
586 <https://doi.org/10.1029/2006JC003551>, 2007.
- 587
- 588

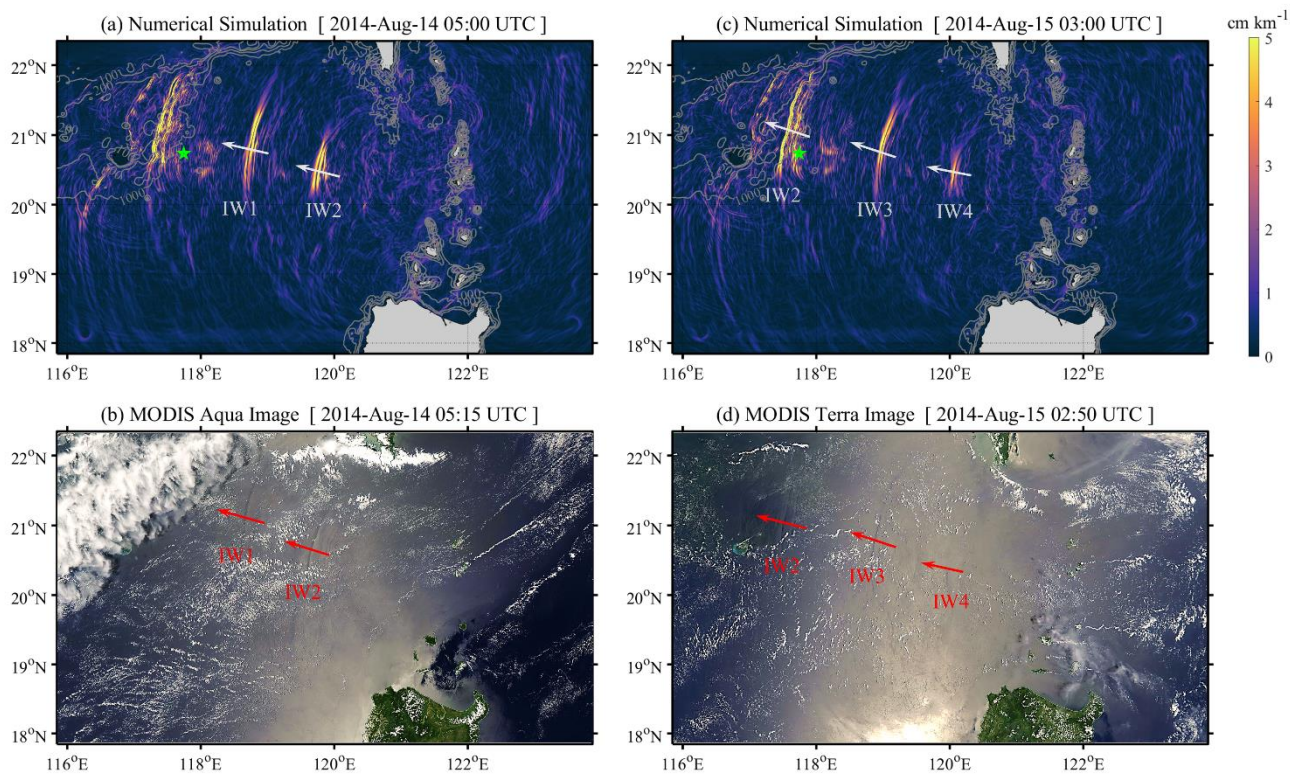


590 **Figure 1.** (a) Bathymetry map of model domain in the northern South China Sea with a mooring station DS (marked as magenta star) in the vicinity of Dongsha Atoll and the transects in two-dimensional models, among which Exp. *2D_500m_8HARs* is in black dashed line while Exps. *2D_500m_8HARs_005N* and *2D_500m_8HARs_005S* are in red dashed lines. (b) Initial temperature and salinity profiles. (c) Density profile. (d) Buoyancy frequency profile. Note the black and red lines in (b-d) represent the data derived from the WOA18 and in-situ observations, respectively.



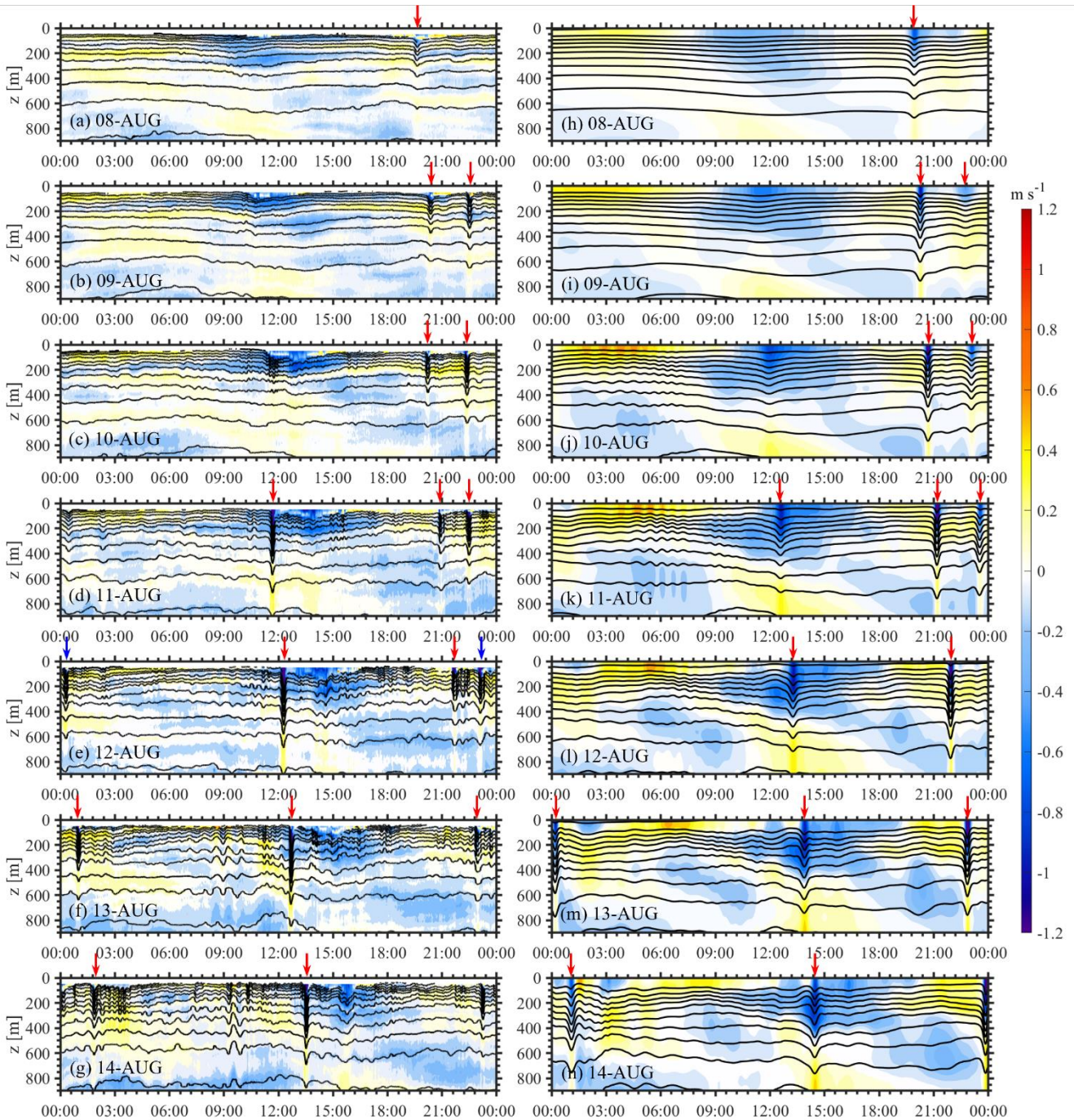
595

Figure 2. Absolute root-mean-square errors of zonal barotropic velocity (U_{bt}) between the model (500m_8HARs_BT) and the TPX08-Atlas dataset for M2 (a), S2 (b), K1 (c), and O1 (d). (e) Reconstructed time series of zonal barotropic velocity at station DS (marked as magenta star in Fig. 2a) of Exp. 500m_8HARs_BT (black line) versus measured data (red line) obtained by eight key tidal constituents.



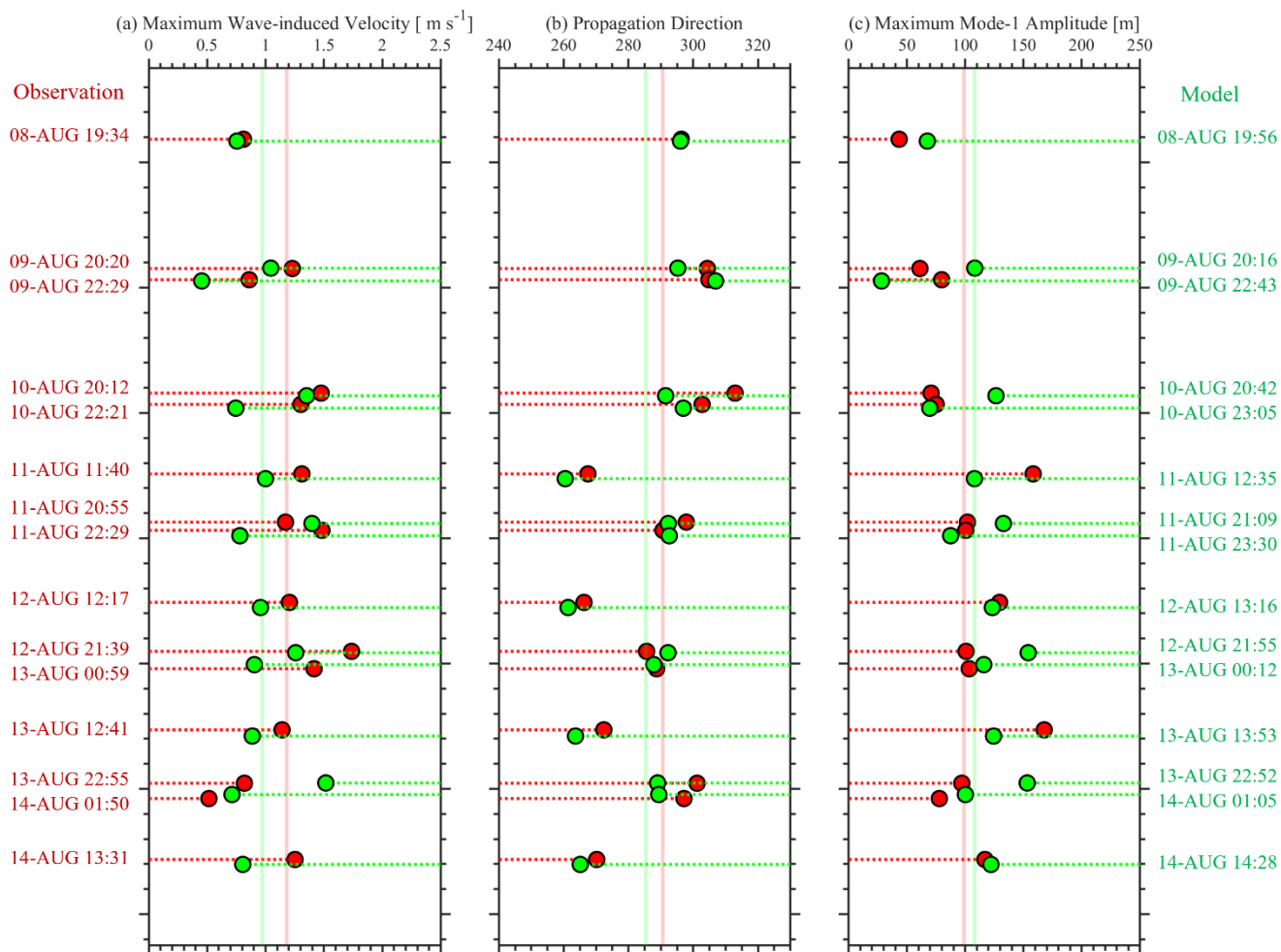
600

Figure 3. (a) Sea surface height gradients induced by internal solitary waves (ISWs) at 05:00 UTC on 14 August 2014 and (b) MODIS-Aqua image obtained at 05:15 UTC on 14 August 2014. (c) Same as (a) but at 03:00 UTC on 15 August 2014. (d) Same as (b) but for MODIS-Terra at 02:50 UTC on 15 August 2014. Note that the MODIS images in (b) and (d) are freely downloaded from the NASA Worldview application (<https://worldview.earthdata.nasa.gov>, open source).



605

Figure 4. (a - g) Temperature isotherms (contours) and baroclinic velocities (shades) in the wave propagation direction from 08 August to 14 August at station DS from in-situ observation. (h - n) Same as (a - g) but for the model (*500m_8HARs*). Red arrows indicate ISWs that model captured, while blue arrows present the missed ones.



610 **Figure 5.** Maximum wave-induced velocities (a), propagation directions (b) and maximum mode-1 wave amplitudes (c) of fifteen ISWs at station DS from in-situ observations (red) and numerical models (green). Averaged values are shown by solid lines.

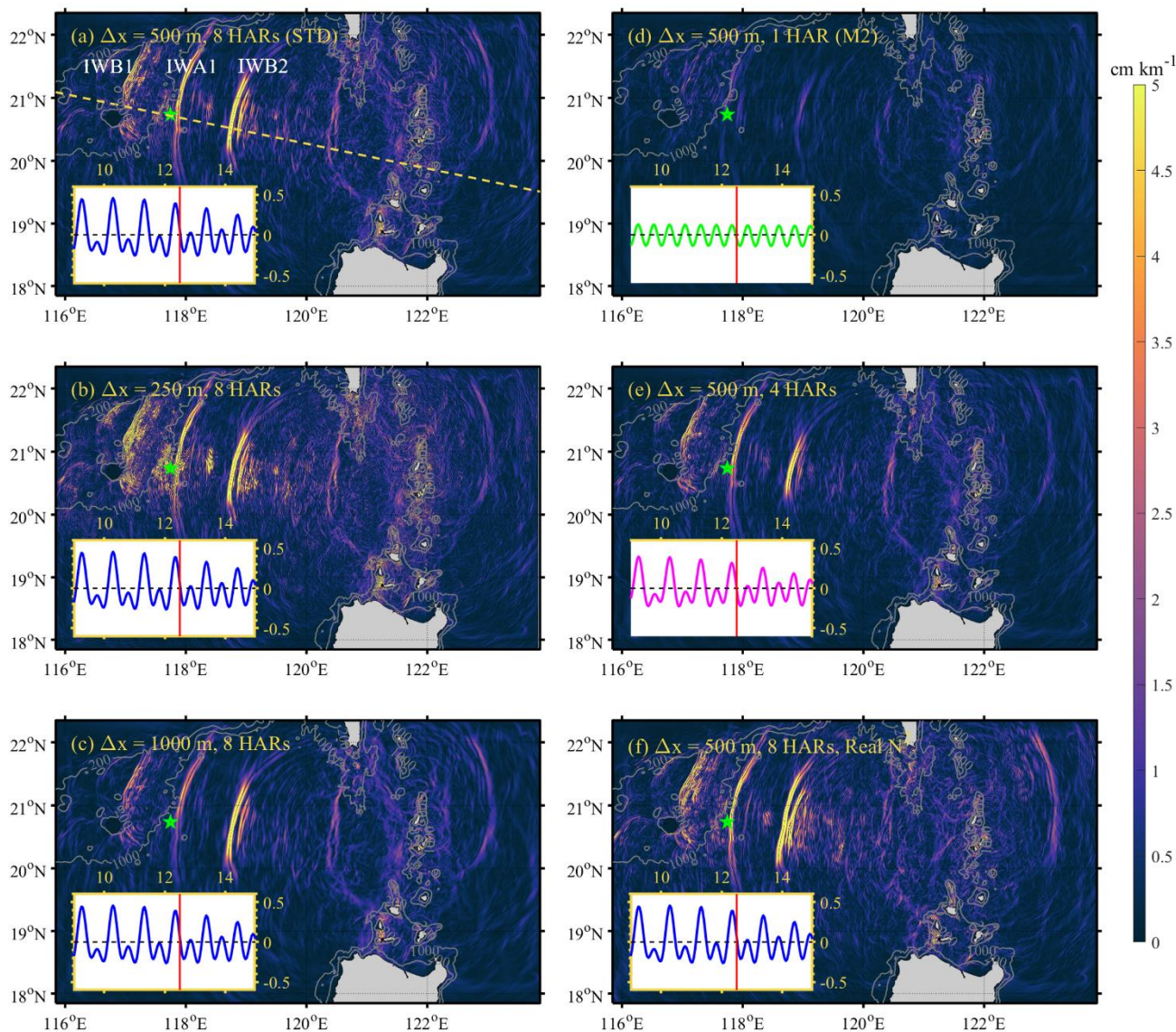


Figure 6. Sea surface height gradients at 12:00 UTC on 12 August 2014 in the model (a) *500m_8HARs*, (b) *250m_8HARs*,
 615 (c) *1000m_8HARs*, (d) *500m_1HAR*, (e) *500m_4HARs*, and (f) *500m_Real_N2*. Note that dashed line in (a) is selected
 transect to present vertical structure of ISWs. Small panels on the bottom left indicate the zonal barotropic velocity (unit in m s^{-1}) in the Luzon Strait with the solid lines showing the tidal conditions at the selected time.

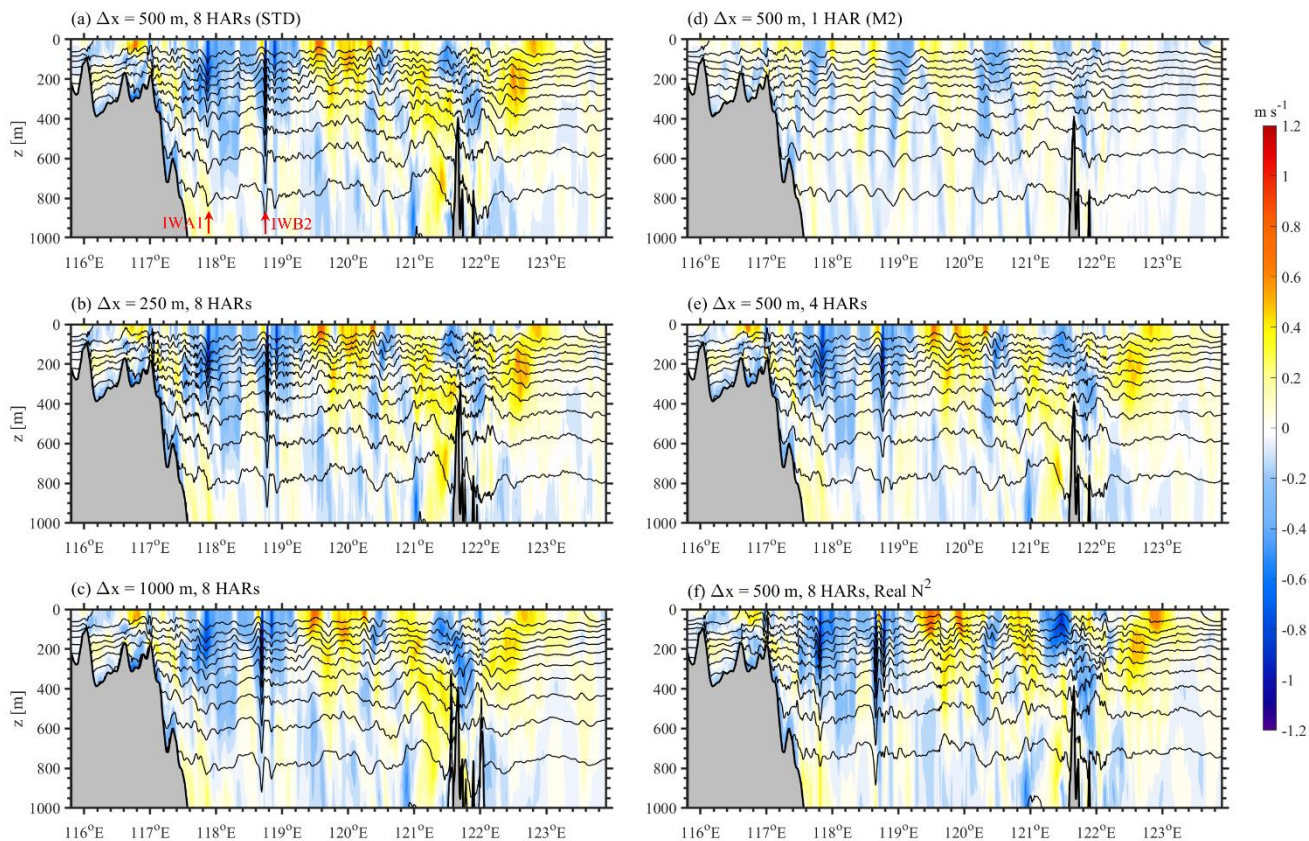


Figure 7. Temperature isotherms (contours) and baroclinic velocities (shades) along the transect (dashed line in Fig. 6a) at 12:00 UTC on 12 August 2014 in the model (a) *500m_8HARs*, (b) *250m_8HARs*, (c) *1000m_8HARs*, (d) *500m_1HAR*, (e) *500m_4HARs*, and (f) *500m_Real_N2*. Note that waves IWA1 and IWB2 are labelled in (a) with red arrows.

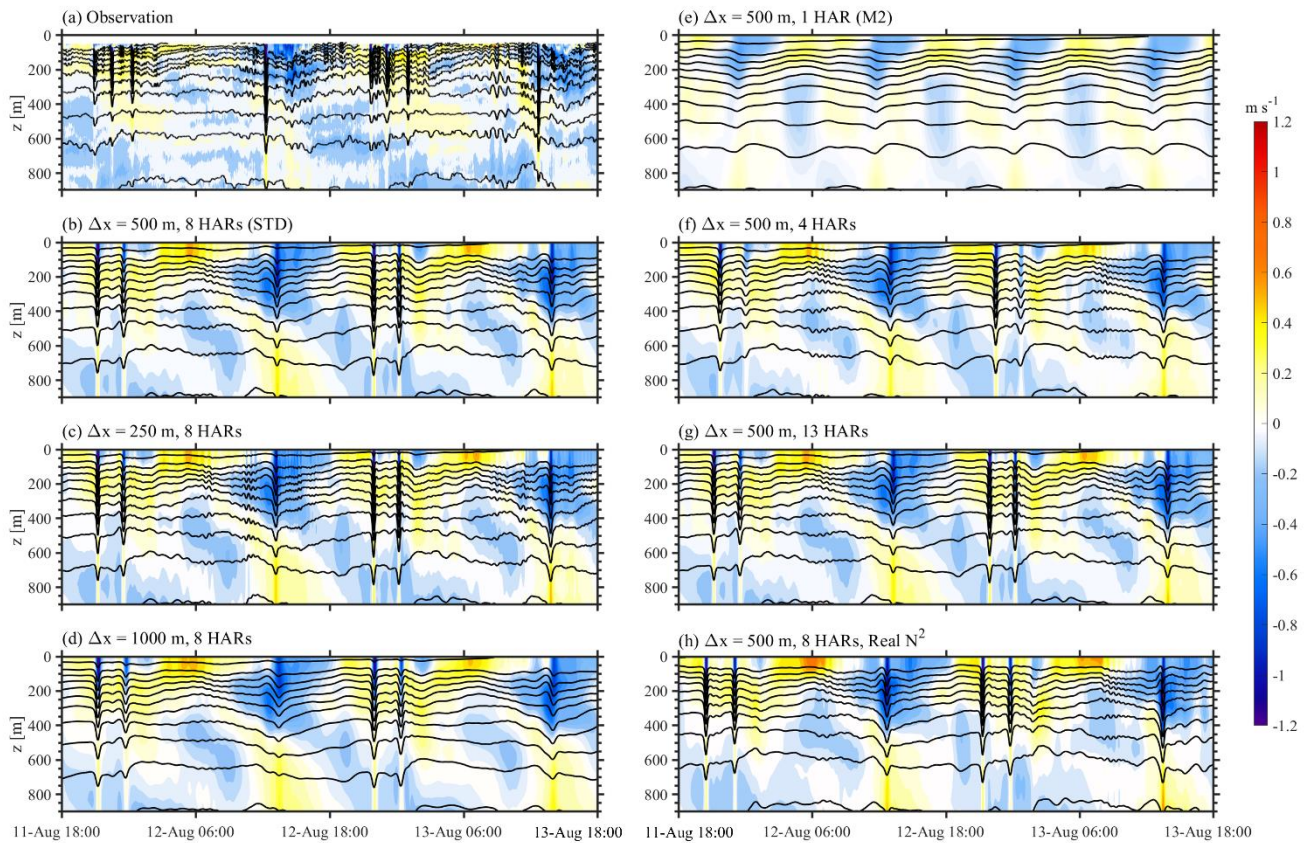


Figure 8. Time series of temperature isotherms (contours) and baroclinic velocities (shades) at station DS from 18:00 UTC on 11 August to 18:00 UTC on 13 August 2014 in the observation (a) and in the model (b) *500m_8HARs*, (c) *250m_8HARs*, (d) *1000m_8HARs*, (e) *500m_1HAR*, (f) *500m_4HARs*, (g) *500m_13HARs*, and (h) *500m_Real_N2*.

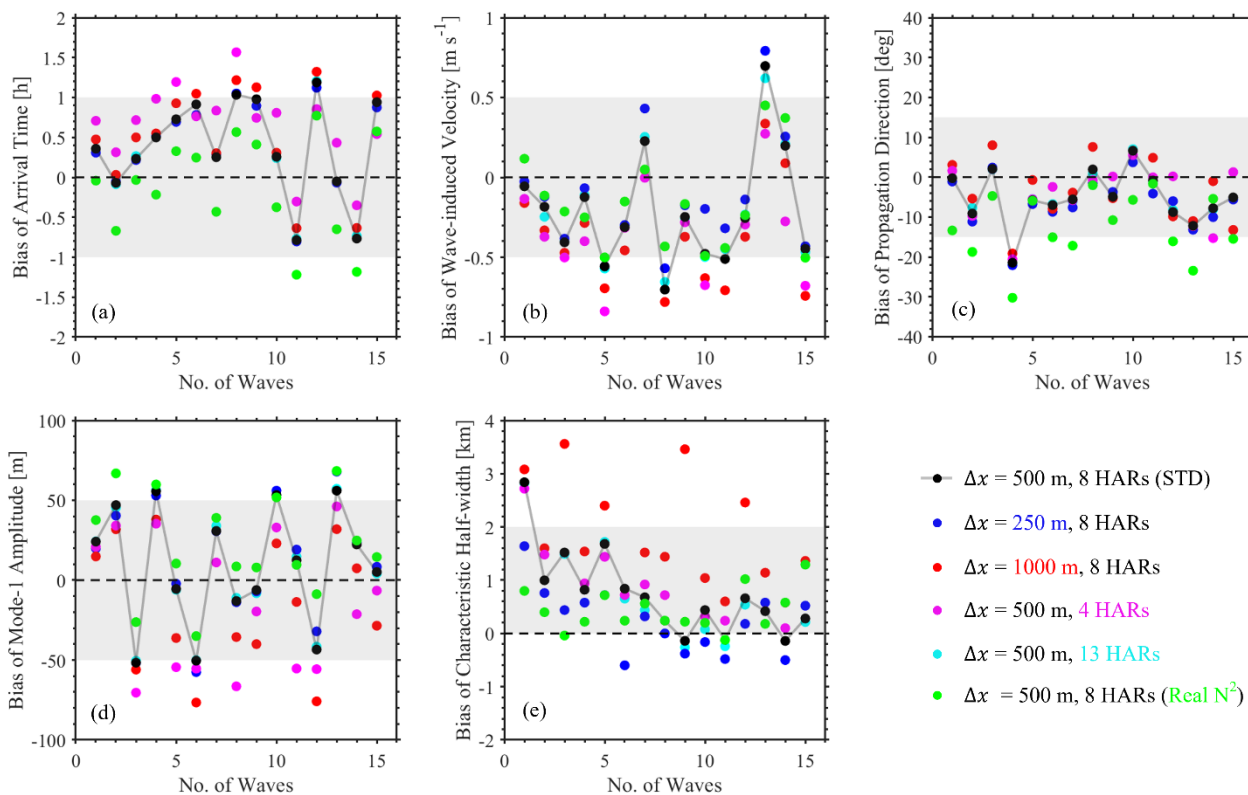
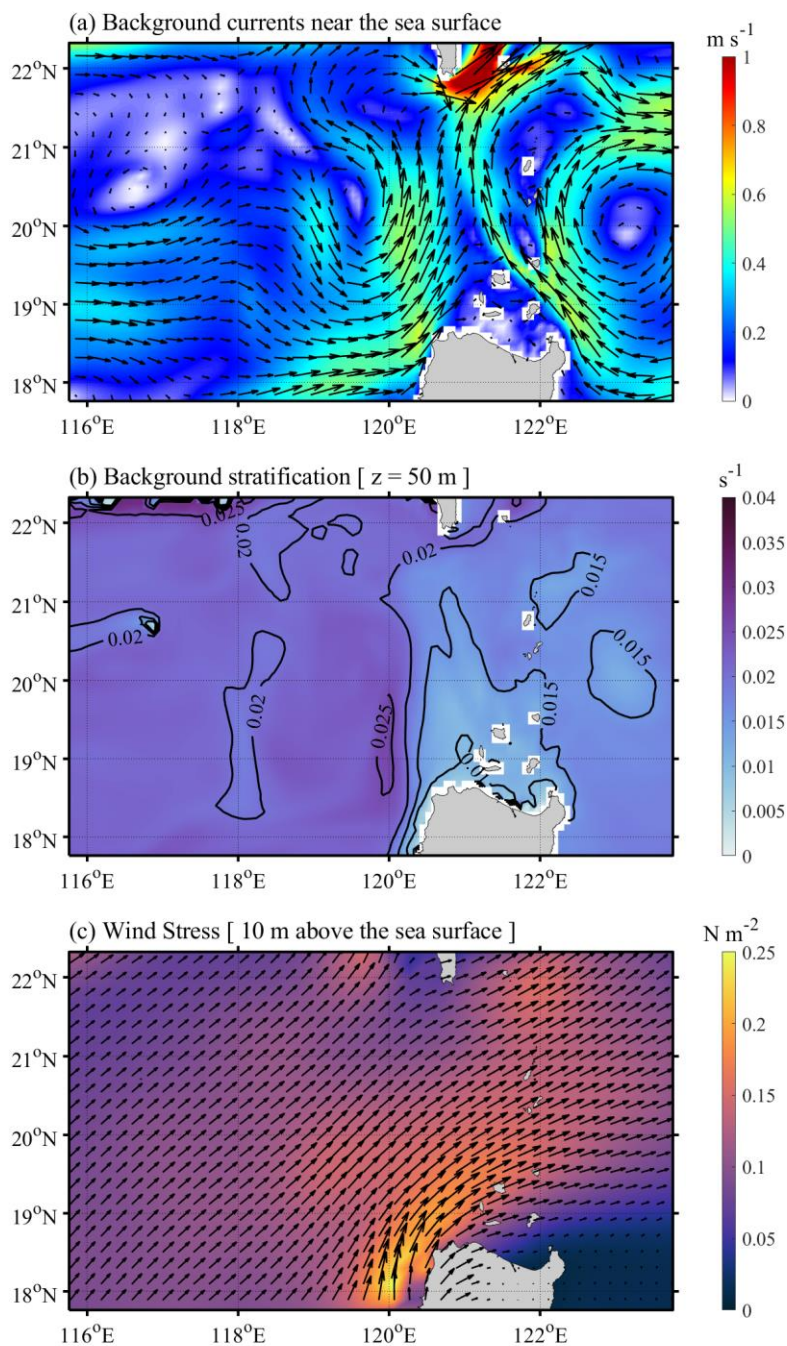
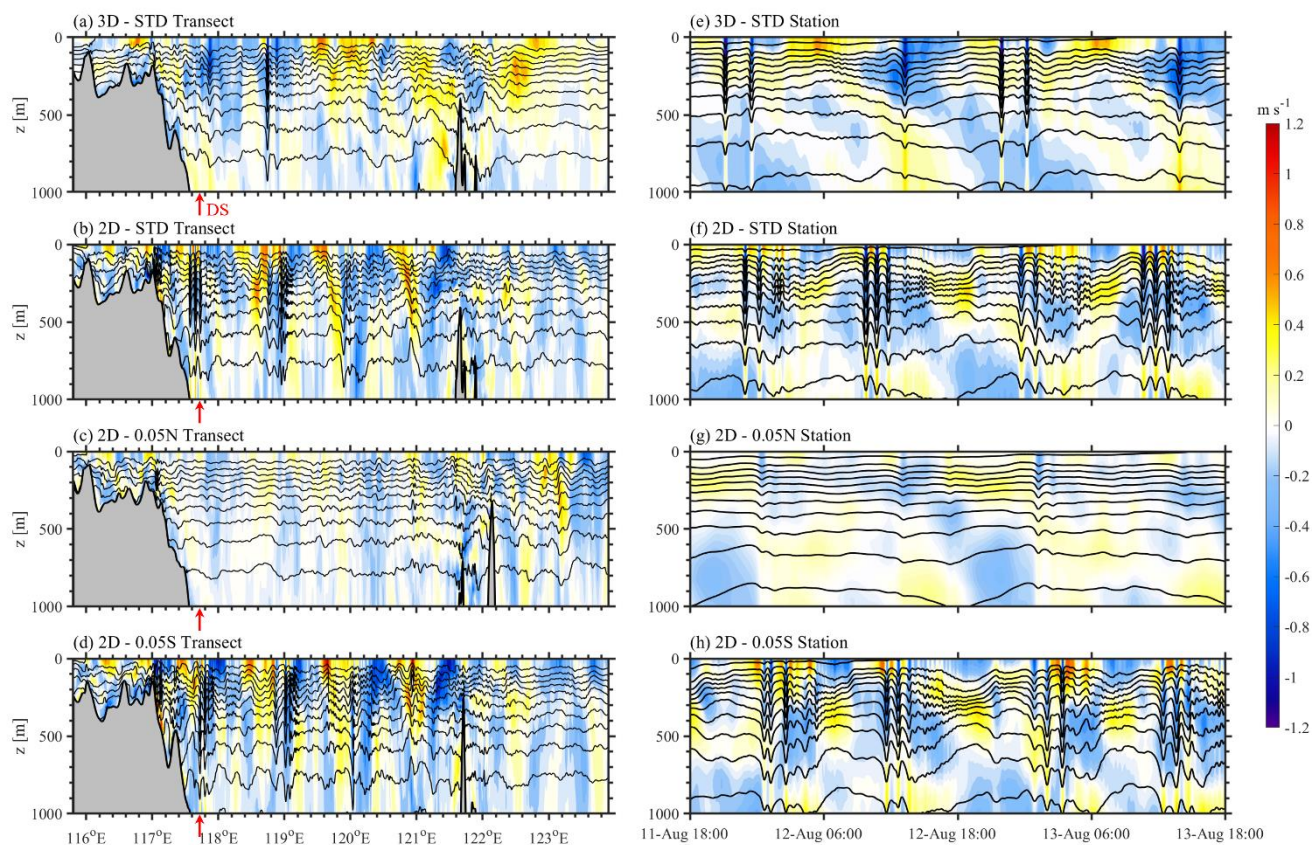


Figure 9. Bias of arrival time (a), maximum wave-induced velocities (b), propagation directions (c), maximum mode-1 wave amplitudes (d), and characteristic half-widths (e) for fifteen ISWs at station DS. Colours present different experiments.



630 **Figure 10.** (a) Background currents near the sea surface (averaged from 05-AUG to 20-AUG 2014, derived from HYCOM dataset). (b) Background buoyancy frequency at a water depth of 50 m. (c) Time-averaged wind stress at 10 m above the sea surface, which is derived from NCEPv2 hourly dataset.



635

Figure A1. Temperature isotherms (contours) and baroclinic velocities (shades) along the transect at 12:00 UTC on 12 August 2014 in the three-dimensional model (a) *500m_8HARs*, in the two-dimensional model (b) *2D_500m_8HARs*, (c) *2D_500m_8HARs_005N*, and (d) *2D_500m_8HARs_005S*. (e – h) Corresponding time series at the stations, which are marked as red arrows in (a – d).

640



Table 1. Summary of previous three-dimensional non-hydrostatic models for internal solitary waves in the northern South China Sea, which are discussed in the text. Further details can be found in the references.

References	Model	Resolution	Tidal constituents	Model domain
Vlasenko et al. (2010) Guo et al. (2011)	MITgcm	$\Delta x = 250$ m, $\Delta y = 1000$ m	8 HARs	118.0° – 122.5°E 20.0° – 21.0°N
Zhang et al. (2011)	SUNTANS	~1358 m (75 – 4740 m)	8 HARs	115.0° – 124.0°E 18.0° – 23.0°N
Alford et al. (2015)	MITgcm	250 m	8 HARs	119.6° – 122.3°E 18.8° – 21.8°N
Lai et al. (2019)	FVCOM	~200 – 500 m (near the shoreline) ~3 km (shelf-slope region)	8 HARs	105.0° – 130.0°E 12.0° – 30.0°N
Zeng et al. (2019)	MITgcm	$\Delta x = 150$ m, $\Delta y = 300$ m	8 HARs	115.5° – 124.5°E 17.5° – 22.5°N



Table 2. Summary of all experimental configurations.

No.	Experiment name	Grid spacing	Tidal forcing	Stratification
1	<i>500m_8HARs</i>	500 m	8 HARs (M2, S2, N2, K2, K1, O1, P1, Q1)	WOA18
2	<i>500m_8HARs_BT</i>	500 m	8 HARs	-
3	<i>250m_8HARs</i>	250 m	8 HARs	WOA18
4	<i>1000m_8HARs</i>	1000 m	8 HARs	WOA18
5	<i>500m_1HAR</i>	500 m	1 HAR (M2)	WOA18
6	<i>500m_4HARs</i>	500 m	4 HARs (M2, S2, K1, O1)	WOA18
7	<i>500m_13HARs</i>	500 m	13 HARs (M2, S2, N2, K2, K1, O1, P1, Q1, M4, MS4, MN4, MM, MF)	WOA18
8	<i>500m_Real_N2</i>	500 m	8 HARs	DS Station



Table 3. Root mean square deviation (RMSD) of wave properties between field observation and 3D sensitivity simulations at the mooring station in the vicinity of the Dongsha Atoll.

No.	Experiment name	RMSD of arrival time [h]	RMSD of wave-induced velocity [m s^{-1}]	RMSD of propagation direction [$^{\circ}$]	RMSD of mode-1 wave Amplitude [m]	RMSD of characteristic half-width [km]
1	<i>500m_8HARs</i>	0.71	0.41	8.35	37.27	1.07
2	<i>500m_8HARs_BT</i>	-	-	-	-	-
3	<i>250m_8HARs</i>	0.67	0.38	8.89	38.12	0.64
4	<i>1000m_8HARs</i>	0.79	0.49	8.54	40.28	2.41
5	<i>500m_1HAR</i>	-	-	-	-	-
6	<i>500m_4HARs</i>	0.81	0.58	8.22	43.69	1.10
7	<i>500m_13HARs</i>	0.71	0.40	8.23	37.36	1.01
8	<i>500m_Real_N2</i>	0.62	0.34	14.74	37.88	0.58